Geosci. Model Dev. Discuss., https://doi.org/10.5194/gmd-2018-254
Manuscript under review for journal Geosci. Model Dev.
Discussion started: 13 November 2018

Geoscientific Model Development
Discussions
Open Access

The Beijing Climate Center Climate System Model (BCC-CSM): Main Progress from CMIP5 to CMIP6

Tongwen Wu[1*], Yixiong Lu[1], Yongjie Fang[1], Xiaoge Xin[1], Laurent Li[1,2], Weiping Li[1], Weihua Jie[1], Jie Zhang[1], Yiming Liu[1], Li Zhang[1], Fang Zhang[1], Yanwu Zhang[1], Fanghua Wu[1], Jianglong Li[1], Min Chu[1], Zaizhi Wang[1], Xueli Shi[1], Xiangwen Liu[1], Min Wei[3], Anning Huang[4], Yaocun Zhang[4], Xiaohong Liu[1,5]

[1]Beijing Climate Center, China Meteorological Administration, Beijing, China
[2]Laboratoire de Météorologie Dynamique, IPSL, CNRS, Sorbonne Université, Paris, France
[3]National Meteorological Information Center, China Meteorological Administration, Beijing, China
[4]Nanjing University, Nanjing, China
[5]University of Wyoming, Laramie, WY, United States

Correspondence to: Tongwen Wu (twwu@cma.gov.cn)

Abstract. Main progresses of Beijing Climate Center (BCC) climate system model from the phase five of the Coupled Model Intercomparison Project (CMIP5) to its phase six (CMIP6) are presented, in terms of physical parameterizations and models performance. BCC-CSM1.1 and BCC-CSM1.1m are the two models involved in CMIP5, and BCC-CSM2-MR, BCC-CSM2-HR, and BCC-ESM1.0 are the three models configured for CMIP6. Historical simulations from 1851 to 2014 from BCC-CSM2-MR (CMIP6) and from 1851 to 2005 from BCC-CSM1.1m (CMIP5) are used for models assessment. The evaluation matrices include (a) energy budget at top of the atmosphere, (b) surface air temperature, precipitation, and atmospheric circulation for global and East Asia regions, (c) sea ice extent and thickness and Atlantic Meridional Overturning Circulation (AMOC), and (d) climate variations at different time scales such as global warming trend in the 20th century, stratospheric quasi-biennial oscillation (QBO), Madden-Julian Oscillation (MJO) and diurnal cycle of precipitation. Compared to

Geosci. Model Dev. Discuss., https://doi.org/10.5194/gmd-2018-254
Manuscript under review for journal Geosci. Model Dev.
Discussion started: 13 November 2018

BCC CMIP5 models, BCC CMIP6 models show significant improvements in many aspects including: tropospheric air temperature and circulation at global and regional scale in East Asia, climate variability at different time scales such as QBO, MJO, diurnal cycle of precipitation, and long-term trend of surface air temperature.

1. Introduction

Changes of global climate and environment are main challenges that human societies are facing for sustainable developments. Climate and environment changes are often the consequence of combined effects of anthropogenic influences and complex interactions among the atmosphere, hydrosphere, lithosphere, cryosphere and biosphere of the Earth system. To better understand behaviors of the earth climate, and to predict its future evolution, appropriate new concepts and relevant methodologies should be proposed and developed. Climate system models are effective tools to simulate the interactions and feedbacks in an objective manner, and to explore their impacts on climate and climate change. Many climate models in the world have been developed since the IPCC-AR4, More than 30 models participated in the CMIP5 project and created an unprecedented dynamics in the scientific community to generate climate information and make them available for scientific researches. Many of these models were then extended into Earth System models by including the representation of biogeochemical cycles. BCC effectively contributed to CMIP5 by running most of the mandatory simulations.

The first generation of Beijing Climate Center ocean-atmosphere Coupled Model BCC-CM1.0 was developed from 1995 to 2004 (e.g. Ding et al., 2002). It was mainly used for seasonal climate prediction. Since 2005, BCC initiated the development of a new fully-coupled climate modelling platform (Wu et al., 2010, 2013, 2014). In 2012, two versions of the BCC model were released: BCC-CSM1.1 with a coarse horizontal resolution T42 (approximately 280 km) and BCC-CSM1.1m with a medium horizontal resolution T106 (approximately 110 km). It was a fully-coupled model with ocean, land surface, atmosphere, and sea-ice components (Wu et al., 2008; Wu, 2012; Xin et al., 2013). Both versions were extensively used for the phase five of the Coupled Model Intercomparison Project (CMIP5, Taylor et al., 2012). At the end of 2017, the second generation of the BCC model was released to run different simulations proposed by the phase six of the Coupled Model Intercomparison Project

(CMIP6, Eyring et al., 2016). The purpose of this paper is to document the main efforts and progress achieved in BCC for its climate model transition from CMIP5 to CMIP6. We show improvements in both model resolution and its physics. A relevant description on model transition is shown in Sections 2 and 3. A comparison of models performance is presented in Section 4.

2. Transition of the BCC climate system model from CMIP5 to CMIP6

Table 1 shows a summary of different BCC models or versions used for CMIP5 and CMIP6. All of them are fully-coupled global climate models with four components, atmosphere, ocean, land surface and sea-ice, interacting with each other. They are physically coupled through fluxes of momentum, energy, water at their interfaces. The coupling was realized with the NCAR flux Coupler version 5. BCC-CSM1.1 and BCC-CSM1.1m are the two models involved in CMIP5. They differ only by their horizontal resolutions. BCC-CSM2-MR, BCC-CSM2-HR, and BCC-ESM1.0 are the three models developed for CMIP6.

BCC-ESM1.0 is our Earth System configuration. It is a global fully-coupled climate-chemistry-carbon model, and intended to conduct simulations for the Aerosol Chemistry Model Intercomparison Project (AerChemMIP, Collins et al., 2017) and the Coupled Climate–Carbon Cycle Model Intercomparison Project (C4MIP, Jones et al., 2016), both endorsed by CMIP6. Its performance is presented in a separated paper (Wu et al., to be submitted). BCC-CSM2-HR, also presented separately, is our high-resolution configuration prepared for conducting simulations of the High Resolution Model Intercomparison Project (HighResMIP v1.0, Haarsma et al., 2016).

In this paper, we focus on BCC-CSM1.1m and BCC-CSM2-MR which are representative of our climate modelling efforts in CMIP5 and CMIP6 respectively. They have the same horizontal resolution (T106, about 110×110 km in the atmosphere and 30×30 km in the tropical ocean), ensuring a fair comparison. But they have different vertical resolutions in the atmosphere (Table 1), which are 26 layers in BCC-CSM1.1m and 46 in BCC-CSM2-MR. The present version of BCC-CSM2-MR takes 50% more computing time than BCC-CSM1.1m for the same amount of parallel computing processors.

2.1 Atmospheric component BCC-AGCM

The atmospheric component of BCC-CSM1.1m is BCC-AGCM2.2 (second generation). It is detailed in a series of publications (Wu et al., 2008, 2010; Wu, 2012; Wu et al., 2013).

BCC-AGCM3-MR is its updated version (third generation), used as the atmosphere component in BCC-CSM2-MR. Table 2 summarizes the main differences of model physics of our atmospheric GCMs between BCC-AGCM2.2 and BCC-AGCM3-MR. Some details are as follows:

a. Deep convection parameterization

Our second-generation atmospheric model, BCC-AGCM2.2, operates with a parameterization scheme of deep cumulus convection developed by Wu (2012). Main characteristics can be summarized as follows:

(1) Deep convection is initiated at the level of maximum moist static energy above the boundary layer. It is triggered when there is positive convective available potential energy (CAPE) and if the relative humidity of the air at the lifting level of convective cloud is greater than 75%;

(2) A bulk cloud model taking into account processes of entrainment/detrainment is used to calculate the convective updraft with consideration of budgets for mass, dry static energy, moisture, cloud liquid water, and momentum. The scheme is also considered the lateral entrainment of the environmental air into the unstable ascending parcel before it rises to the lifting condensation level. The entrainment/detrainment amount for the updraft cloud parcel is determined according to the increase/decrease of updraft parcel mass with altitude. Based on a total energy conservation equation of the whole adiabatic system involving the updraft cloud parcel and the environment, The mass change for the adiabatic ascent of the cloud parcel with altitude is derived;

(3) The convective downdraft is assumed to be saturated and originated from the level of minimum environmental saturated equivalent potential temperature within the updraft cloud;

(4) The closure scheme determining the mass flux at the base of convective cloud is that suggested by Zhang (2002). It assumes that the increase/decrease of CAPE due to changes of the thermodynamic states in the free troposphere resulting from convection approximately balances the decrease/increase resulting from large-scale processes.

A modified version of Wu (2012) is used in BCC-AGCM3-MR for deep convection parameterization. The convection is triggered only when the boundary layer is unstable or there exists updraft velocity in the environment at the lifting level of convective cloud, and simultaneously there is positive CAPE. This modification is aimed to connect the deep convection to the instability of the

Geosci. Model Dev. Discuss., https://doi.org/10.5194/gmd-2018-254
Manuscript under review for journal Geosci. Model Dev.
Discussion started: 13 November 2018

Geoscientific Model Development Discussions
Open Access

boundary layer. The lifting condensation level is set to above the nominal level of non-divergence (600 hPa) in BCC-AGCM2.2 and lowered to the level of 650 hPa in BCC-AGCM3-MR. These modifications in the deep convection scheme are found to improve the simulation of diurnal cycle of precipitation and Madden-Julian Oscillation (MJO).

b. Cloud fraction

In BCC-AGCM2.2, the total cloud cover (C_{tot}) within each model grid is set as the maximum value of three cloud covers: low-level marine stratus (C_{mst}), convective cloud (C_{conv}), and stratus cloud (C_s),

$$C_{tot} = \max\left(C_{conv}, C_{mst}, C_s\right) \tag{1}$$

As in CAM3, the marine stratocumulus cloud is diagnosed with an empirical relationship between the cloud fraction and the boundary layer stratification which is evaluated with atmospheric variables at surface and 700mb (Klein and Hartmann [1993]). The convective cloud fraction uses a functional form of Xu and Krueger [1991] relating the cloud cover to updraft mass flux from the deep and shallow convection schemes. The stratus cloud fraction is diagnosed on the basis of relative humidity which varies with pressure.

A new cloud scheme is developed and used in BCC-AGCM3-MR. It consists of calculating convective cloud and the total cloud cover in a different way from BCC-AGCM2.2. The total cloud fraction at each model grid is given as

$$C_{tot} = C_{conv} + \left(1 - C_{conv}\right) \cdot \max\left(C_{mst}, C_s\right) \tag{2}$$

And the convective cloud $\mathrm{C_{conv}}$ is assumed to be the sum of shallow ($C_{shallow}$) and deep (C_{deep}) convective cloud fractions:

$$C_{conv} = C_{shallow} + C_{deep} \tag{3}$$

$C_{shallow}$ and C_{deep} are non-overlapped with each other and diagnosed following the relationships,

$$C_{conv} q^*\left(T_c\right) + \left(1 - C_{conv}\right)\overline{q} = \overline{q}_{conv} \tag{4}$$

$$C_{conv} T_c + \left(1 - C_{conv}\right)\overline{T} = \overline{T}_{conv} \tag{5}$$

and

Geosci. Model Dev. Discuss., https://doi.org/10.5194/gmd-2018-254
Manuscript under review for journal Geosci. Model Dev.
Discussion started: 13 November 2018

$$q^*(T_c) = q^*(\overline{T}) + \frac{\partial q^*(\overline{T})}{\partial \overline{T}}(T_c - \overline{T}) \tag{6}$$

where $\bar{q}$ and $\overline{T}$, $\bar{q}_{conv}$ and $\overline{T}_{con\square}$ denote the model grid box-averaged water vapor mixing ratio and temperature in the 'environment' before and after convection activity, respectively. T_c and $q^*(T_c)$ are the temperature inside the convective cloud plume and its saturated water vapor mixing ratio. If no supersaturation exists in clouds, we obtain

$$C_{conv} = \frac{(\bar{q}_{conv} - \bar{q}) - \frac{\partial q^*(\overline{T})}{\partial \overline{T}}(\overline{T}_{conv} - \overline{T})}{q^*(\overline{T}) - \bar{q}} \tag{7}$$

The temperature T_c and the specific humidity $q_c = q^*(T_c)$ of the cloud plume can be firstly derived from Eqs. (5) and (6). Following the method above, the cloud fraction (C_{deep} and $C_{shallow}$), temperature (T_{deep} and $T_{shallow}$), specific humidity (q_{deep} and $q_{shallow}$) for the deep convective, shallow convective clouds can be then deduced sequentially.

After the three moisture processes (i.e. deep convection, shallow convection, and stratiform precipitation) are finished, and the mean temperature ($\overline{T}_{box}$) and specific humidity ($\bar{q}_{box}$) of the model-grid box are updated, temperature ($\overline{T}_{ambient}$) and specific humidity ($\bar{q}_{ambient}$) in the ambient outside the convective clouds can be estimated using the following Eqs.,

$$\bar{q}_{box} = \bar{q}_{ambient} \cdot (1 - C_{deep} - C_{shallow}) + q_{deep} \cdot C_{deep} + q_{shallow} \cdot C_{shallow}, \tag{8}$$

and

$$\overline{T}_{box} = \overline{T}_{ambient} \cdot (1 - C_{deep} - C_{shallow}) + T_{deep} \cdot C_{deep} + T_{shallow} \cdot C_{shallow}. \tag{9}$$

Finally, the stratus cloud fraction C_S is diagnosed on the basis of the relative humidity ($RH_{abmient}$) of the ambient,

$$C_s = \left(\frac{RH_{ambient} - RH_{min}}{1 - RH_{min}}\right)^2 \tag{10}$$

where RH_{min} is a threshold of relative humidity and $RH_{abmient}$ is derived with $\overline{T}_{ambient}$ and $\bar{q}_{ambient}$.

c. Indirect effects of aerosols on clouds and precipitation

Indirect effects of aerosols were not included in our models for CMIP5. That is, the cloud droplets effective radius was not related to aerosols, neither the precipitation efficiency. The cloud droplets effective radius was either prescribed or a simple function of atmospheric temperature, as in the Community Atmosphere Model (CAM3, Collins et al., 2004). The effective radius for warm clouds was specified to be 14 μm over open ocean and sea ice, and was a function of atmospheric temperature over land. For ice clouds, the effective radius was also a function of temperature following Kristj´ansson and Kristiansen [2000].

Aerosol particles influence clouds and the hydrological cycle by their ability to act as cloud condensation nuclei and ice nuclei. This indirect radiative forcing of aerosols is included in the latest version of BCC-AGCM3-MR, with the effective radius of liquid water cloud droplets being related to the cloud droplet number concentration N_{cdnc} (cm^{-3}). As proposed by Martin et al. (1994), the volume-weighted mean cloud droplet radius $r_{l,vol}$ can be expressed as

$$r_{l,vol} = \left[(3LWC) / (4\pi\rho_w N_{cdnc}) \right]^{1/3}, \tag{11}$$

where ρ_w is the liquid water density, LWC is the cloud liquid water content (g cm^{-3}). Cloud water and ice contents are prognostic variables in our model with source and sink terms taking into account the cloud microphysics. The effective radius of cloud droplets r_{el} is then estimated as

$$r_{el} = \beta \cdot r_{l,vol} \tag{12}$$

where β is a parameter dependent on the droplets spectral shape. There are various methods to parameterize it (e.g. Pontikis and Hicks, 1992; Liu and Daum, 2002). We use the calculation proposed by Peng and Lohmann (2003),

$$\beta = 0.00084 N_{cdnc} + 1.22 \tag{13}$$

In BCC-AGCM3-MR, the liquid cloud droplet number concentration N_{cdnc} (cm^{-3}) is a diagnostic variable dependent on aerosols mass. It is explicitly calculated with the empirical function suggested by Boucher and Lohmann (1995) and Quaas et al. (2006) :

$$N_{cdnc} = \exp\left[5.1 + 0.41 \ln(m_{aero}) \right] \tag{14}$$

The total aerosols mass is the sum of four types of aerosol,

Geosci. Model Dev. Discuss., https://doi.org/10.5194/gmd-2018-254
Manuscript under review for journal Geosci. Model Dev.
Discussion started: 13 November 2018

Geoscientific Model Development
Open Access
Discussions

$$m_{aero} = m_{SS} + m_{OC} + m_{SO_4} + m_{NH_4NO_2} \,. \tag{15}$$

Here, m_{aero} (μ g.m^{-3}) is the total mass of all hydrophilic aerosols, i.e., the first bin (0.2 to 0.5 μ m) of sea salt (m_{SS}), hydrophilic organic carbon (m_{OC}), sulphate (m_{SO_4}), and nitrate ($m_{NH_4NO_4}$). Nitrate as a rapidly increasing aerosol species in recent years affects present climate and potentially has large implications on climate change (Xu and Penner, 2012; Li et al., 2014). A dataset of nitrate from NCAR CAM-Chem (Lamarque et al., 2012) is used in our model.

Aerosols also exert impacts on precipitation efficiency (Albrecht, 1989), which is taken into account in the parameterization of non-convective cloud processes. We use the same scheme as in CAM3 (Rasch and Kristj´ansson, 1998; Zhang et al., 2003). There are five processes that convert condensate to precipitate: auto-conversion of liquid water to rain, collection of cloud water by rain, auto-conversion of ice to snow, collection of ice by snow, and collection of liquid by snow. The auto-conversion of cloud liquid water to rain (PWAUT) is dependent on the cloud droplet number concentration and follows a formula that was originally suggested by Chen and Cotton [1987],

$$PWAUT = C_{l,aut}\hat{q}_l^2 \rho_a / \rho_w \left(\frac{\hat{q}_l \rho_a}{\rho_w N_{ncdc}} \right)^{1/3} H\left(r_{l,vol} - r_{lc,vol}\right) \tag{16}$$

Where $\hat{q}_l$ is in-cloud liquid water mixing ratio, ρ_a and ρ_w are the local densities of air and water respectively, and

$$C_{l,aut} = 0.55\pi^{1/3} k \left(3/4\right)^{4/3} \left(1.1\right)^4 . \tag{17}$$

In which k = 1.18 × 106 cm^{-1} sec^{-1} is the Stokes constant. H(x) is the Heaviside step function with the definition,

$$H(x) = \begin{cases} 0, & x < 0 \\ 1, & x \geq 0 \end{cases} \tag{18}$$

$r_{lc,vol}$ is the critical value of mean volume radius of the liquid cloud droplets $r_{l,vol}$, and set to 15 μ m.

d. Parameterization of gravity wave drag

Gravity waves can be generated by a variety of sources including orography, convection, and geostrophic adjustment in regions of baroclinic instability (Richter et al., 2010). Gravity waves propagate upward from their source regions and break when large amplitudes are attained. This produces a drag on the mean flow. Gravity wave drag plays an important role in explaining the zonal mean flow and thermal structure in the upper atmosphere.

In previous versions of BCC models, the orographic gravity wave drag was parameterized as in McFarlane (1987), but non-orographic sources were not considered. In BCC-AGCM3-MR, the gravity wave drag generated from convective sources is introduced as in Beres et al. (2004). The key point of the Beres scheme is relating the momentum flux phase speed spectrum to the convective heating properties. In the present version of BCC-AGCM3-MR, the convective gravity wave parameterization is activated only when the deep convective heating depth is greater than 2.5 km.

The uncertainty in the magnitude of momentum flux arises from the horizontal scale of the heating and the convective fraction. The convective fraction (CF) within a grid cell is an important parameter and can be tuned to obtain right wave amplitudes. Previous studies of Alexander et al. (2004) show that CF can vary from ~0.2% to ~7%–8%. We use 5% in BCC-AGCM3-MR. This parameterization scheme of convective gravity waves can improve the model's ability to simulate the stratospheric quasi-biennial oscillation in BCC-AGCM3-MR.

2.2 Land component BCC-AVIM

BCC-AVIM, Beijing Climate Center Atmosphere-Vegetation Interaction Model, is a comprehensive land surface scheme developed and maintained in BCC. The version 1 (BCC-AVIM1.0) was used as the land component in BCC-CSM1.1m participating in CMIP5 (Wu et al., 2013). It includes major land surface biophysical and plant physiological processes. Its origin could go back to the Atmosphere-Vegetation Interaction Model (AVIM) (Ji, 1995; Ji et al., 2008) with the necessary framework to include biophysical, physiological, and soil carbon-nitrogen dynamical processes. The biophysical module in BCC-AVIM1.0, with 10 layers for soil and up to five layers for snow, is almost the same as that used in the NCAR Community Land Model version 3 (CLM3) (Oleson et al., 2004). The terrestrial carbon cycle in BCC-AVIM1.0 consists of a series of biochemical and physiological processes modulating photosynthesis and respiration of vegetation. Carbon assimilated by vegetation is parameterized by a seasonally varying allocation of carbohydrate to leaves, stem, and root tissues as a function of the prognostic leaf area index. Litter due to turnover and mortality of vegetation, and carbon dioxide release into atmosphere through the heterogeneous respiration of soil microbes is taken into account in BCC-AVIM1.0. Vegetation litter falls to the ground surface and into the soil is divided into eight idealized terrestrial carbon pools according to the timescale of carbon decomposition of each pool and transfers among different pools, which is similar to that in CEVSA model (Cao and Woodward, 1998).

BCC-AVIM1.0 has been updated to BCC-AVIM2.0 which serves as the land component of BCC-CSM2-MR participating in CMIP6. As listed in Table 2, several improvements have been implemented in BCC-AVIM2.0, such as the inclusion of a variable temperature threshold to determine soil water freezing/thawing rather than fixed at 0°C, a better calculation of snow surface albedo and snow cover fraction, a dynamic phenology for deciduous plant function types, and a four-stream approximation on solar radiation transfer through vegetation canopy. Besides, a simple scheme for surface fluxes over rice paddy is also implemented in BCC-AVIM2.0. These improvements are briefly discussed as follows.

(a) Soil water freezes at the constant temperature 0°C in BCC-AVIM1.0, but the actual freezing-thawing process is a slowly and continuously changing process. We take into account the fact that the soil water potential remains in equilibrium with the water vapor pressure over pure ice when soil ice is present. Based on the relationships among soil water matrix potential ψ (mm), soil temperature and soil water content, a variable temperature threshold for freeze-thaw dependent on soil liquid water content, soil porosity and saturated soil matrix potential is introduced. The inclusion of this scheme improves the performance of BCC-AVIM2.0 in the simulation about seasonal frozen soil (Xia et al., 2011).

(b) In BCC-AVIM1.0, we took into account the snow aging effect on surface albedo with a simple consideration by using a unified scheme to mimic the snow surface albedo decrease with time. In BCC-AVIM2.0, we assume different reduction rates of snow albedo with actual elapsed time after snowfalls in the accumulating and melting stages of a snow season (Chen et al., 2014). Besides, the variability of sub-grid topography is now taken into account to calculate the snow cover fraction within a model grid cell.

(c) Unlike the empirical plant leaf unfolding and withering dates prescribed in BCC-AVIM1.0, a

Geosci. Model Dev. Discuss., https://doi.org/10.5194/gmd-2018-254
Manuscript under review for journal Geosci. Model Dev.
Discussion started: 13 November 2018

dynamic determination of leaf unfolding, growth, and withering dates according to the budget of photosynthetic assimilation of carbon similar to the phenology scheme in CTEM (Arora, 2005) was implemented in BCC-AVIM2.0. Leaf loss due to drought and cold stresses in addition to natural turnover are also considered.

(d) The four-stream solar radiation transfer scheme within canopy in BCC-AVIM2.0 is based on the same radiative transfer theory used in atmosphere (Liou, 2004). It adopts the analytic formula of Henyey-Greenstein for the phase function. The vertical distribution of diffuse light within canopy is related to transmisivity and reflectivity of leaves, besides, average leaf angle and direction of incident direct beam radiation influence diffuse light within canopy as well. The upward and downward radiative fluxes are determined by the phase function of diffuse light, G-function, leaf reflectivity and transmisivity, leaf area index, and the cosine of solar angle of incident direct beam radiation (Zhou et al., 2018).

(e) Considering the wide distribution of rice paddies in Southeast Asia and the quite different characteristics of rice paddies and bare soil, a simple scheme about the surface albedo, roughness length, turbulent sensible and latent heat fluxes over rice paddies is developed and implemented in BCC-AVIM2.0

(f) Finally, land-use and land-cover changes are explicitly involved in BCC-AVIM2.0. An increase in crop area implies the replacement of natural vegetation by crops, which is often known as deforestation.

2.3 Ocean and Sea Ice

There are no significant changes for the ocean and sea ice from BCC-CSM1.1m to BCC-CSM2-MR. But for the sake of completeness, we present here a short description of them. The oceanic component is MOM4-L40, an oceanic GCM. It was based on the Z-coordinate Modular Ocean Model (MOM), version 4 (Griffies, 2005) developed by the Geophysical Fluid Dynamics Laboratory (GFDL). It has a nominal resolution of 1°×1° with a tri-pole grid, the actual resolution being from 1/3° latitude between 30°S and 30°N to 1.0° at 60° latitude. There are 40 z-levels in the vertical. The two northern poles of the curvilinear grid are distributed to land areas over Northern America and over the Eurasian continent. There are 13 vertical levels placed between the surface and the 300-m depth of the upper ocean. MOM4_L40 adopts some mature parameterization schemes, including Swedy's tracer-based third order advection scheme, isopycnal tracer mixing and diffusion scheme (Gent and McWilliams, 1990), Laplace horizontal friction scheme, KPP vertical mixing scheme (Large et al., 1994), complete convection scheme (Rahmstorf, 1993), overflow scheme of topographic processing of sea bottom boundary/steep slopes (Campin & Goosse, 1999), and shortwave penetration schemes based on spatial distribution of chlorophyll concentration (Sweeney et al., 2005).

Concentration and thickness of sea ice are calculated by the Sea Ice Simulator (SIS) developed by GFDL (Winton, 2000). It is a global sea ice thermodynamic model including the Elastic–Viscous–Plastic dynamic process and Semtner's thermodynamic process. SIS has 3 vertical layers, including 1 snow cover and 2 ice layers of equal thickness. In each grid, 5 categories of sea ice (including open water) are considered, according to the thickness of sea ice. It also takes into account the mutual transformation from one category to another under thermodynamic conditions. The sea ice model operates on the same oceanic grid and has the same horizontal resolution of MOM_L40. SIS calculates concentration, thickness, temperature, salinity of sea ice and motions of snow cover and ice sheet. There is no gas exchange through sea ice.

2.4. Surface turbulent fluxes between air and sea/sea ice

The atmosphere and sea/sea ice interplay through the exchange of surface turbulent fluxes of momentum, heat and water. An optimum treatment of the surface exchange, sound in physics and economic in computation, is very important in simulating the climate variability. During the past years, we maintain a continuous effort to improve the turbulent exchange processes between air and sea/sea ice in different versions of BCC models.

In BCC-CSM1.1m, the bulk formulas of turbulent fluxes over sea surface originate from those used in CAM3, with some modifications to the roughness lengths and corrections to the temperature and moisture gradients considering sea spray effects (Wu et al., 2010). The bulk formulas are updated in BCC-CSM2-MR. The coefficients in roughness lengths calculations were adjusted and the arbitrary gradient corrections are not used. Instead, a gustiness parameterization is included to account for the subgrid wind variability that is contributed by boundary layer eddies, convective precipitation, and cloudiness (Zeng et al., 2002).

Geosci. Model Dev. Discuss., https://doi.org/10.5194/gmd-2018-254
Manuscript under review for journal Geosci. Model Dev.
Discussion started: 13 November 2018

Geoscientific Model Development Discussions

In terms of turbulent exchange between air and sea ice, we proposed a new bulk algorithm aiming to improve flux parameterizations over sea ice (Lu et al., 2013). Based on theoretical and observational analysis, the new algorithm employs superior stability functions for stable stratification as suggested by Zeng et al. (1998), and features varying roughness lengths. All the three roughness lengths (z_0, z_T, z_Q) of sea ice were set to a constant (0.5 mm) in BCC-CSM1.1m. Observational studies show that values of z_0 tend to be smaller than 0.5 mm over sea ice in winter and larger than 0.5 mm in summer (Andreas et al., 2010a; Andreas et al., 2010b). In the new parameterization used in BCC-CSM2-MR, the roughness lengths for momentum differentiate between warm and cold seasons. For simplicity, z_0 is treated as

$$z_0(mm)=\begin{cases}0.1 & \text{for } T_s \le -2°C \\ 0.8 & \text{for } T_s > -2°C\end{cases}, \tag{19}$$

where T_s represents surface temperature. For the scalar roughness lengths, a theoretical-based model proposed by Andreas (1987) is used in the new scheme. This model expresses the scalar roughness z_s (z_T or z_Q) as a function of the roughness Reynolds number R*, i.e.,

$$\ln(z_s/z_0)=b_0+b_1(\ln R_*)+b_2(\ln R_*)^2. \tag{20}$$

Andreas (1987, 2002) tabulates the polynomial coefficients b_0, b_1 and b_2.

3. Experimental design

Simulations presented in this work follow the protocols defined by CMIP5 and CMIP6. We pay attention for them to be comparable in spite of showing the transition of our climate system model from CMIP5 to CMIP6. The principal simulation to be analyzed is the historical simulation (hereafter historical) with prescribed forcings from 1850 to 2005 for CMIP5 (to 2014 for CMIP6).

Historical forcings data are based as far as possible on observations and downloaded from the webpage (https://esgf-node.llnl.gov/search/input4mips/). They mainly include: (1) GHG concentrations (only CO_2, N_2O, Ch_4, CFC11, CFC12 used in BCC models) with zonal-mean values and updated monthly; (2) Yearly global gridded land-use forcing; (3) Solar forcing; (4) Stratospheric aerosols (from volcanoes); (5) CMIP6-recommended anthropogenic aerosol optical properties which is formulated in terms of nine spatial plumes associated with different major anthropogenic source regions (Stevens et al., 2017). (6) Time-varying gridded ozone concentrations. In addition, aerosol masses based on CMIP5 (Taylor et al., 2012) are used for on-line calculation of cloud droplet effective radius in BCC model.

The preindustrial climate state of BCC-CSM2-MR is preceded by a more than 500 years piControl simulation following the requirement of CMIP6. The initial state of the piControl simulation itself is obtained through individual spin-up runs of each component of BCC-CSM2-MR.

4. Evaluation and comparison between BCC CMIP5 and CMIP6 models

4.1 Global Energy Budget

Radiative fluxes at the up-limit of the atmosphere are fundamental variables characterizing the Earth's energy balance. Satellite observations in modern time allow us to monitor changes in the net radiation at top-of-atmosphere (TOA) from 2001 onwards. CERES (Clouds and Earth's Radiant Energy System) project, with the lessons learned from its predecessor, the Earth's Radiation Budget Experiment (ERBE), provides improved observation-based data products of Earth's radiation budget (Wielicki et al, 1996). Recently, data of CERES are synthesized with EBAF (Energy Balanced and Filled) data to derive the CERES-EBAF products, suitable for evaluation of climate models (Loeb et al., 2012). With the CERES/EBAF data, we obtain a quasi-equilibrium (0.81 W m^{-2}) of Earth's radiative budget at TOA for the period of 2003 to 2014. As listed in Table 4, globally-averaged TOA net energy is 0.85 W m^{-2} in BCC-CSM2-MR and 0.98 W m^{-2} in BCC-CSM1.1m for the period from 1981 to 2014. It means that the whole earth system in our models is very close to energy equilibrium. The TOA shortwave and longwave components in BCC-CSM2-MR are generally closer to CERES/EBAF than those in BCC-CSM1.1m.

Clouds constitute a major modulator of the radiative transfer in the atmosphere for both solar and terrestrial radiations. Their macro and micro properties, including their radiative properties exert strong impacts on the equilibrium and variation of the radiative budget at TOA or at surface. Figure 1 displays annual and zonal mean of shortwave, longwave and net cloud radiative forcing for BCC CMIP5 (blue curves), CMIP6 (red curves) models and observations (black curves). Model results are for the period 1986–2005, while the available CERES-EBAF data are for 2003–2014. Although they cover different time periods, they are still relevant to reveal climatological mean performance of climate models. In low latitudes between 30S and 30N, BCC-CSM1.1m shows excessive cloud radiative forcing for both shortwave and longwave radiations. These biases are reduced in BCC-CSM2-MR. Cloud radiative forcing in the mid latitudes in BCC-CSM2-MR seems, nevertheless, overestimated for the shortwave radiation. It is clear that the new physics modifies the simulated climate and cloud properties, including the fractional coverage of clouds, their vertical distribution as well as their liquid water and ice content.

4.2 Behaviors of the atmosphere at present day

Biases of annual mean surface air temperature (at 2 meters) for BCC-CSM2-MR and BCC-CSM1.1m are shown in Figure 2. In both BCC models, biases are generally within ±3°C, but there are slightly systematic warm biases over oceans from 50° S to 50°N and systematic cold ones over most land regions in north of 50°N, in East Asia and in North Africa. Cold biases in high latitudes of the Northern Hemisphere (North Atlantic, Arctic, North America and Siberia) seem amplified in BCC-CSM2-MR. In the Southern Ocean, both models show a strong warm area in the Weddell Sea. BCC-CSM1.1m shows cold biases in other regions of the Southern Ocean.

Figure 3 shows model biases of annual-mean precipitation for BCC-CSM1.1m and BCC-CSM2-MR. They are very close from each other. Their RMSE is also very close: 1.12 mm/day against 1.18 mm/day. Excessive rainfalls in Tropical Africa, in the Indian Ocean, in the Maritime Continent seem amplified in BCC-CSM2-MR. Regions of lack of precipitation, such as North India, South China, the two sides of Sumatra, and the Amazon, experience significant amelioration in the new model.

We now use the Taylor diagram (Figure 4) to evaluate the general performance of our two models in terms of temperature at 850hPa, precipitation and atmospheric general circulation. The evaluation is done against climatology of ERA-Interim dataset for the period of 1986 to 2005 (Dee et al., 2011).

For global fields, we calculate the spatial pattern correlations between models and NCEP dataset for the annual-mean climatology of sea level pressure (SLP), precipitation (PRCP), temperature at 850 hPa level (T850), wind velocity at 850 hPa (U850 and V850) and at 200 hPa (U200), and geopotential height at 500hPa (Z500) over the period 1980–2000. Except for precipitation and zonal wind at 850 hPa which have lower correlation (less than 0.90) with observation, correlations for other variables are all above 0.90. The pattern correlation of geopotential height at 500hPa with NCEP is 0.995, the best correlation among these variables. Except for V850, correlations of all other variables in CMIP6 model version (BCC-CSM2-MR) have an evident improvement compared to CMIP5 version (BCC-CSM1.1m). The normalized standard deviations of most variables except for the precipitation and T850 are obviously improved in BCC-CSM2-MR. As a whole, the performances of most variables in BCC-CSM2-MR are better than those in BCC-CSM1.1m.

Results shown in the Taylor diagrams in Figure 4s about improvements in surface climate and atmospheric general circulation at different vertical levels are consistent with improvements in the vertical distribution of atmospheric temperature. Figure 5 shows the yearly-averaged zonal mean of atmospheric temperature biases in BCC-CSM2-MR and BCC-CSM1.1m, with ERA-Interim for the period of 1986–2005 as reference. Overall, both BCC-CSM2-MR and BCC-CSM1.1m have similar biases in their vertical structure, with 1–3 K warmer in the stratosphere (above 100 hPa) for most of the domain equatorward of 70°N and 70°S. There are larger cold biases near the tropopause (centered near 200hPa) for southward of 30°S and northward of 30°N. In the middle to lower troposphere (below 400hPa), there is a warm bias of 1-2K. Improvements in BCC-CSM2-MR are mainly located in the troposphere below 100 hPa. Both cold biases near the tropopause in high latitudes and warm bias in lower latitudes are reduced.

The improvement in tropospheric temperature induces naturally smaller biases for the zonal wind in the whole troposphere in BCC-CSM2-MR (Figure 5). But there are still westerly wind biases of 6 $m.s^{-1}$ in the layer of 100-200 hPa in the tropics. Westerly jets at mid-latitudes are slightly too strong in both hemispheres.

Given a much higher vertical resolution and an advanced parameterization of the gravity wave drag, the new model BCC-CSM2-MR is able to represent the stratospheric quasi-biennial oscillation (QBO), as shown in Figure 6 which displays time-height diagrams of the tropical zonal winds averaged from 5°S to 5°N. The three panels show observations from the ERA-Interim reanalysis and relevant simulation results from the two models in CMIP6 and CMIP5. Figure 6(a) shows alternative westerlies and easterlies in the lower stratosphere appearing with a mean period of about 28 months in the ERA-Interim reanalysis. In Figure 6(b), the BCC-CSM2-MR simulations present a clear quasi-biennial oscillation of the zonal winds as observed. In this study, the QBO period is taken as the time between easterly and westerly wind transitions at 20 hPa. The simulation produces about 12 QBO cycles from 1980 to 2005. The average period is 24.6 months, whereas the shortest and longest cycles last for 18 and 35 months, respectively. ERA-Interim values are 27.9, 23, and 35 months for average, minimum, and maximum cycle length. The observed asymmetry in amplitude with the easterlies being stronger than the westerlies is reproduced in the simulated zonal winds. At 20 hPa, the simulated easterlies often exceed -20 m s^{-1}, while in the reanalysis easterly winds peak at -30 to -40 m s^{-1}. Simulated westerlies of the QBO range from 8 to 12 m s^{-1}, whereas the reanalysis show peak winds of 16 to 20 m s^{-1}. The amplitudes of the QBO cycles in the simulation are weaker than in the reanalysis, implying that the forcing is less adequate to drive the QBO. The downward propagation of the simulated QBO phases occurs in a regular manner, but does not penetrate to sufficiently low altitudes. In the BCC-CSM1.1m simulations shown in Figure 6(c), however, the QBO is inexistent and only a semiannual oscillation of easterlies can be found.

Madden-Julian Oscillation (MJO) is a very important atmospheric variability acting within a periodicity between 20 and 100 days in the tropics with considerable effects on regional weather and climate. It exerts significant impacts on monsoonal circulations and organization of tropical rainfalls. From the tropical Indian Ocean to the Western Pacific, MJO shows a pronounced behavior of eastward propagation, as shown in Figure 7a, in the form of longitude-time, the lagged correlation coefficient of the rainfall in the eastern Indian Ocean (75–85°E; 5°S–5°N) with other positions and with lagged time. We can easily observe the eastward-propagating characteristic, with a moving velocity estimated at 5 m s^{-1}. As shown in a comparison work of Jiang et al. (2015), three fourth of CMIP5 models don't show the propagation behavior, with only a standing oscillation when data are filtered to retain only the 20-100 day variability. Figure 7b and 7c show the same plot, but from our two models in CMIP5 and CMIP6. Although the new model is far from realistic in terms of eastward propagation, there is indeed a clear improvementcompared to the old one.

MJO can also exert impacts on weather and climate of extra-tropics, either through emanation of Rossby waves, or the poleward propagation of MJO itself. Figure 7d shows a latitude-time diagram for lagged correlation coefficients when rainfalls are filtered to only retain the variability of 20-100 days. Figure 7e and 7f are the counterpart simulated by our two models. The new model presents a clear improvement.

4.3 Sea ice state and oceanic overturning circulation

Figure 8 shows the seasonal cycle of sea ice extent (SIE) and thickness in the two Polar Regions in

Geosci. Model Dev. Discuss., https://doi.org/10.5194/gmd-2018-254
Manuscript under review for journal Geosci. Model Dev.
Discussion started: 13 November 2018

our models. Observation from the National Snow and Ice Data Center (NSIDC) and the European Centre for Medium-Range Weather Forecasts (ECMWF) are also plotted for the purpose of comparison. Observations from NSIDC show that Arctic sea ice cover reaches a minimum extent of 7.74×10^6 km^2 in September and rises to a maximum extent of 15.79×10^6 km^2 in March (Fig. 8a). The two models can both capture the seasonal variation and pattern, but large biases exist in magnitude, especially in boreal winter. As to Antarctic SIE, the ice cover undergoes a very large seasonal cycle, which is similar to observations. However, the SIE in BCC-CSM1.1m is too extensive throughout the year, particularly in southern hemisphere winter. Comparatively, the new model BCC-CSM2-MR simulates a relatively smaller seasonal cycle and reduced ice cover in all months which is closer to observations. As to ice thickness, the two models simulate a thinner ice cover compared to observations in all seasons for both Arctic and Antarctic. The most remarkable improvements of BCC-CSM2-MR appear in the boreal warm seasons, especially from June to September with thicker ice presented in the Arctic Ocean.

The Atlantic Meridional Overturning Circulation (AMOC) plays a significant role in driving the global climate variation (Caesar et al., 2018). AMOC consists of two primary overturning cells. In the upper cell, warm water flows northward in the upper 1000 m to supply the formation of the North Atlantic Deep Water (NADW), which returns southward in the depth range of approximately 1500 to 4000 m. In contrast, in the lower cell, the Antarctic Bottom Water (AABW) flows northward in the Atlantic basin beneath NADW. Figure 9 shows the time-averaged AMOC simulated by the two coupled model versions. The two main cells are well depicted. The lower branch of NADW is much deeper in BCC-CSM2-MR than in BCC-CSM1.1m, as indicated by the depth of the zero-contour line. Moreover, the central intensity of NADW in BCC-CSM2-MR is over 22.5 Sv, about 2.5 Sv stronger than that in BCC-CSM1.1m.

4.4. Performance in Simulating the Global Warming in the 20th Century

The historical simulation allows us to evaluate the ability of models to reproduce the global warming and climate variability in the 20th century. The performance depends on both model formulation and the time-varying external forcings imposed on the models (Allen et al., 2000). Figure 10 presents global-mean (from 60° S to 60°N) surface air temperature evolutions from HadCRUT4 (Morice et al., 2012) and BCC CMIP5 and CMIP6 models. To better reveal long-term trends, the climatological mean is calculated for the reference period 1961–1990 and removed from the time series. The interannual variability of both simulations is qualitatively comparable to that observed. When a 9-year smoothing is applied, the long-term trend of both CMIP6 and CMIP5 models is highly correlated with HadCRU. The correlation coefficients are 0.90 in CMIP5 and 0.93 CMIP6, respectively.

A remarkable feature in Figure 10 is the presence of a global warming hiatus or pause for the period from 1998 to 2013 when the observed global surface air temperature warming slowed down. This is a hot topic, largely debated in the scientific research community (e.g. Fyfe et al., 2016; Medhaug et al., 2017). Our CMIP6 model can capture this warming hiatus. Another warming hiatus occurred in the period of 1942 to 1974. BCC models only capture the warming slowdown in the late period from 1958 to 1974. The reason why the BCC CMIP6 model captures both periods of global warming hiatus will be explored in other paper.

The models response of the SAT to volcanic forcing is slightly stronger than that estimated with HadCRU data. Evident global cooling shocks are coincident with significant volcanic eruptions such as Krakatoa (in 1883), West Indies Agung (in 1963), and Mount Pinatubo (in 1991). Each of these volcanic eruptions significantly enriched stratospheric aerosols (available from http://data.giss.nasa.gov/modelforce/strataer/). As shown in Figure 2c, SAT may decrease by up to 0.4°C within 1 to 2 years after major volcanic eruptions. The substantial cooling respone to volcanic eruptions is, to a great extent, due to the aerosol direct radiative forcing too strong in both versions of BCC-CSM.

Figure 11 shows time-series of minimum sea-ice extent from 1851 to 2012 for (a) the Arctic in September and (b) the Antarctic in March as simulated in BCC-CSM2-MR and BCC-CSM1.1m. Observation-based NSIDC data are also plotted when available. The Arctic sea-ice extent in BCC-CSM2-MR is slightly improved, in comparison to BCC-CSM1.1m. But the Antarctic minimum sea-ice extent in the new model is very small, almost a third of what observed. The old model had however a more realistic behavior for this regard. This discrepancy is related to too-warm temperatures simulated in BCC-CSM2-MR in the Southern Ocean, in particular in the Weddell Sea. The downward trend in the Arctic summer sea-ice extent is, however, better simulated in the new model than in the old one.

4.5 Climate sensitivity to CO_2 increasing

Climate sensitivity is an emblematic parameter to characterize the sensitivity of a climate model to external forcing, with all feedbacks included. It generally designates the variation of global mean surface air temperature in response to a forcing of doubled CO_2 concentration in the atmosphere (IPCC 2013). As commonly practiced in the climate modelling community, an equilibrium climate sensitivity and a transient climate response can be separately evaluated, corresponding to a situation of equilibrium and transient states of climate.

We use the standard simulation of 1% CO_2 increase per year (1pctCO_2) to calculate the transient climate response (TCR), while the equilibrium climate sensitivity (ECS) uses the 4xCO_2 abrupt-change simulation by applying the forcing/response regression methodology proposed by Gregory et al. (2004). The TCR is calculated using the difference of annual surface air temperature between the pre-industrial experiment and a 20-year period centered on the time of CO_2 doubling in 1pctCO_2, which is 1.71 for BCC-CSM1.1m and 2.02 for BCC-CSM2-MR. The ECS is diagnosed from the 150-year run of abruptCO2 following the approach of Gregory (2012). The method is based on the linear relationship (Figure 12) governing the changes of net top-of-atmosphere downward radiative flux and the surface air temperature simulated in abrupt 4xCO_2 relative to the pre-industrial experiment. The ECS is equal to a half of the temperature change when the net downward radiative flux reaches zero (Andrews et al., 2012). It is assumed here that 2xCO_2 forcing is half of that for 4xCO_2, hypothesis generally verified in climate models. As shown in Fig. 12, the ECS is 3.03 for BCC-CSM2-MR and 2.89 for BCC-CSM1.1m. So the TCR of the new version model BCC-CSM2-MR is lower than BCC-CSM1.1m, while the ECS of BCC-CSM2-MR is higher than BCC-CSM1.1m.

4.6. Evaluation of models for their performance in East Asia

A good simulation of climate over East Asia is always a challenging issue for the climate modelling community, as the region is under influences of complex topography (high Tibetan Plateau), and atmospheric circulations from low latitudes (tropical monsoon circulation) and from higher latitudes. Figure 13 plots a Taylor diagram over East Asia covering the region (100°-140°E, 20°-50°N). Both BCC-CSM1.1m (blue figures) and BCC-CSM2-MR (red figures) are plotted for precipitation, sea-level pressure and variables of the atmospheric general circulation. There is a clear and remarkable improvement from BCC CMIP5 to CMIP6. The amelioration is both in the spatial pattern correlation (radial lines) and in the ratio of standard deviations (circles from the origin).

The East Asian summer monsoon rainfall has a seasonal progression from south to north at the beginning of summer and then a quick retreat to the south when summer terminates (as shown in Figure 14a). This phenomenon is strongly related to the fact that the East Asian monsoon rainfall takes place in the frontal zone between warm and humid air mass from the south, and cold and dry air mass from the north. This seasonal migration is also accompanied with a meridional movement of the Western North Pacific Subtropical High, an important atmospheric center of action controlling the climate of the region. Figure 14b and 14c compare our two models in terms of seasonal migration of the monsoon rainfall. In the old model, rainfall was too weak. The new model produces more precipitation. In terms of seasonal match, both models show a delay of the peak rainfall by about one month, even longer in BCC-CSM2-MR.

Finally, let us examine the rainfall diurnal cycle in summer. Figure 15 shows the timing of the rainfall diurnal cycle from observation and the two models. Main zones of nocturne rainfall can be recognized in the south flank of the Tibetan Plateau, in the Sichuan Basin in the east of the Tibetan Plateau, and in the north of Xinjiang in Central Asia. There is also a zone of nocturne rainfall in the low reach of the Yellow River. This is mainly under the influence of nocturne rainfall in the area of the Bohai Sea. Other regions over land experience diurnal rainfall peak in the afternoon after 16 hours local time. The diurnal cycle of rainfall was extensively studied in Jin et al. (2013) in terms of physics causing the diurnal cycle. But the good simulation of diurnal cycle is always a major challenge for climate modeling. We can see that it is not very well simulated in our old model and in East China the peak occurs in the mid and later night (0-4 am). But the improvement is quite spectacular in our new model with rainfall peak delayed in the afternoon. Such an improvement is due to the implementation of our new trigger scheme in convection parameterization.

5. Conclusions and discussion

This paper presents the main progress of BCC climate system models from CMIP5 to CMIP6 and focuses on the description of CMIP6 version model BCC-CSM2-MR and CMIP5 version model BCC-CSM1.1m especially on the model physics. Main updates in model physics include a modification of deep convection parameterization, a new scheme for cloud fraction, indirect effects of aerosols on clouds and precipitation, and gravity wave drag generated by deep convection. Surface processes in BCC-AVIM have also been significantly improved for soil water freezing treatment, snow aging effect on surface albedo, and timing of vegetation leaf unfolding, growth, and withering. A four-stream radiation transfer within vegetation canopy is used to replace the two-stream radiation transfer. There is a new treatment for rice paddy waters. New schemes for surface turbulent fluxes of momentum, heat and water in the interface of atmosphere and sea/sea ice are also used.

The evaluation of model performance in simulating present-day climate is presented for main climate variables, such as, surface air temperature, precipitation, and atmospheric circulation for the globe and for East Asia. Emphasis is put on comparison between the CMIP5 and CMIP6 model versions (BCC-CSM2-MR versus BCC-CSM1.1m). The globally-averaged TOA net energy is 0.85 Wm^{-2} in BCC-CSM2-MR, and 0.98 $W m^{-2}$ in BCC-CSM1.1m. Both versions have a very good energy equilibrium. Model biases of excessive cloud shortwave and longwave radiative forcings over low latitudes in BCC-CSM1.1m are obviously reduced in BCC-CSM2-MR. When compared with BCC-CSM1.1m, the spatial patterns of climate means of 2 m surface air temperature, precipitation, and atmospheric general circulation in BCC-CSM2-MR are overall improved at the global scale, particularly at the regional scale in East Asia. These improvements in BCC-CSM2-MR are possibly caused by usage of a new scheme for cloud fraction and consideration of indirect effects of aerosol on clouds and precipitation. The details will be discussed in the other paper. BCC-CSM1.1m has a severe bias in sea ice extent (SIE) and thickness (Tan et al., 2015): too extensive in cold seasons and less extensive in warm seasons in both hemispheres. The most impressive improvements in BCC-CSM2-MR appear in the boreal warm seasons, especially from June to September with thicker ice presented in the Arctic Ocean. However, in the Southern Hemisphere, the sea ice extent and thickness in BCC-CSM2-MR become even systematically smaller than those in its previous version. This is still an issue that needs to be addressed in the future work. There is another model bias of weak oceanic overturning circulation in BCC-CSM1.1m. This bias is reduced in the new version BCC-CSM2-MR, and the strength of AMOC is increased.

Further evaluations are performed on climate variabilities at different time scales, including long-term trend of global warming in the 20th century, QBO, MJO, and diurnal cycle of precipitation. The globally-averaged annual-mean surface air temperature from the historical simulation of BCC-CSM2-MR is much closer to HadCRUT4 observation than BCC-CSM1.1m, and the observed global warming hiatus or warming slowdown in the period from 1998 to 2013 is captured in BCC-CSM2-MR. With a higher vertical resolution and the inclusion of the gravity wave drag generated by deep convection, the new version of BCC-CSM2-MR is able to reproduce the stratospheric QBO, while it does not exist in BCC-CSM1.1m. QBO simulation in BCC-CSM2-MR is related to not only high resolution in the vertical layers but also consideration of gravity wave drag generated by deep convection. It will be discussed in Lu et al. (to be submitted). MJO is a very important atmospheric oscillation and main features are partly improved in BCC-CSM2-MR, but its intensity is still weaker than its counterpart in observation. The rainfall diurnal cycle in China has strong regional variations with pronounced nocturne rainfalls in the Sichuan Basin and in north China near the Bohai Sea. The diurnal rainfall generally peaks in the local time afternoon for most other land regions. BCC-CSM2-MR shows a clear improvement of rainfall diurnal peaks compared to the CMIP5 model (BCC-CSM1.1m). This improvement of rainfall diurnal variation is partly related to the modification of deep convective scheme of Wu (2012), which will be discussed in the other paper.

Finally, we also evaluate the climate sensitivity to CO_2 increasing in the standard simulation of 1% CO_2 increase per year (1pctCO2) and the 4xCO2 abrupt-change. The transient climate response in the new CMIP6 model version BCC-CSM2-MR is lower than that in the previous CMIP5 model BCC-CSM1.1m, while the equilibrium climate sensitivity ECS for BCC-CSM2-MR is slightly higher than its counterpart in BCC-CSM1.1m.

From our model evaluations, we find that although basic feature of the QBO can be simulated in BCC-CSM2-MR, the magnitude between westerly and easterly interchange is still too weak. We also note that there are large biases of air temperature and winds in the stratosphere. Therefore, improvement of the stratospheric temperature and circulation simulations is an important priority in the future development of BCC models. In addition, sea ice simulation in the Antarctic region has large biases, which need to be improved.

6. Code and data availability

Please contact Tongwen Wu (twwu@cma.gov.cn) to obtain the source codes for BCC models. The model output from the CMIP6 historical simulation described in this paper will be distributed through the Earth System Grid Federation (ESGF). As for BCC CMIP5 simulation, the model output will be freely accessible through data portals after registration. Details about ESGF are presented on the CMIP Panel website at http://www.wcrp-climate.org/index.php/wgcm-cmip/about-cmip.

Author contributions

Tongwen Wu lead the BCC-CSM development. Tongwen Wu and Xiaoge Xin designed the experiments and carried them out. Tongwen Wu, Laurent Li, and Xiaohong Liu wrote the final document with contributions from all other authors.

Acknowledgements

This work was supported by The National Key Research and Development Program of China (2016YFA0602100).

References

Albrecht, B.: Aerosols, cloud microphysics, and fractional cloudiness, Science, 245, 1227–1230, 1989.

Adler, R. F., Chang, A.: The Version 2 Global Precipitation Climatology Project (GPCP) Monthly Precipitation Analysis (1979-Present), J. Hydrometeor., 4, 1147–1167, 2003

Alexander, M. J., May, P. T., and Beres, J. H.: Gravity waves generated by convection in the Darwin area during the Darwin Area Wave Experiment, J. Geophys. Res., 109, D20S04, doi: 10.1029/2004JD004729, 2004.

Allen, M., Stott, P., Mitchell, J., Schnur, R., and Delworth, T.: Quantifying the uncertainty in forecasts of anthropogenic climate change, Nature, 407, 617-620, 2000.

Arora, V. K., and Boer, G. J.: A parameterization of leaf phenology for the terrestrial ecosystem component of climate models, Global Change Biology, 11, 39-59, doi:10.1111/j.1365-2486.2004.00890.x, 2005.

Andreas, E. L.: A theory for the scalar roughness and the scalar transfer coefficients over snow and sea ice, Bound.-Layer Meteor., 38, 159-184, 1987.

Andreas, E. L.: Parameterizing scalar transfer over snow and ice: A review, Journal of Hydrometeorology, 3, 417-432, 2002.

Andreas, E. L., Horst, T. W., Grachev, A. A., Persson, P. O. G., Fairall, C. W., and Guest, P. S.,and Jordan, R.E.:

Parametrizing turbulent exchange over summer sea ice and the marginal ice zone, Quartely Journal of the Royal Meteorological Society, 136, 927-943, 2010a.

Andreas, E. L., Persson, P. G., Jordan, R. E., Horst, T.W., Guest, T.S., Grachev, A.A., and Fairall, C.W.: Parameterizing turbulent exchange over sea ice in winter, Journal of Hydrometeorology, 11, 87-104, 2010b.

Andrews, T., Gregory, J. M., Webb, M. J., and, K. E.: Forcing, feedbacks and climate sensitivity in CMIP5 coupled atmosphereocean climate models, Geophys. Res. Lett, 38, L09712, doi: 10.1029/2012GL051607, 2012.

Beres, J. H., Alexander, M. J., and Holton, J. R.: A method of specifying the gravity wave spectrum above convection based on latent heating properties and background wind, J. Atmos. Sci., 61, 324-337, 2004.

Boucher, O., Lohmann, U.: The sulphate-CCN-cloud albedo effect – a sensitivity study with two general circulation models, Tellus 47B, 281–300, 1995.

Caesar, L., Rahmstorf, S., Robinson, A., Feulner, G., Saba, V.: Observed fingerprint of a weakening Atlantic Ocean overturning circulation, Nature, 556, 191-196, 2018.

Campin J.M., and Goosse, H.: Parameterization of density-driven downsloping flow for a coarse-resolution ocean model in z-coordinate, Tellus, 51A, 412–430, 1999.

Cao M., and Woodward F. I.: Net primary and ecosystem production and carbon stocks of terrestrial ecosystems and their responses to climate change, Global Change Biology, 4, 185-198, 1998.

Chen C., and Cotton, W. R.: The physics of the marine stratocumulus-capped mixed layer, J. Atmos. Sci., 44 (50), 2951–2977, 1987.

Chen A., Li, W. P., Li, W. J., and Liu, X.: An observational study of snow aging and the seasonal variation of snow albedo by using data from Col de Porte, France. Chinese Science Bulletin, 59 (34), 4881-4889, 2014

Collins, W. D., Rasch, P.J., Boville, B.A., Hack, J. J., McCaa, J.R., Williamson, D. L., Kiehl, J. T., Briegleb, B., Bitz C., Lin S.J., Zhang, M.H., and Dai, Y.J.: Description of the NCAR community atmosphere model (CAM3). Technical Report NCAR/TN-464 + STR, National Center for Atmospheric Research, Boulder, Colorado, 226 pp, 2004.

Collins, W. J., Lamarque, J.–F., Schulz,M., Boucher, O., Eyring, V., Hegglin, M. I., Maycock, A., Myhre, G., Prather, M., Shindell, D., and Smith, S. J.: AerChemMIP: quantifying the effects of chemistry and aerosols in CMIP6, Geosci. Model Dev., 10, 585–607, 2017.

Dee, D.P., Uppala, S. M., Simmons, A. J., Berrisford, P., Poli, P., Kobayashi, S., Andrae, U., Balmaseda, M. A., Balsamo, G., Bauer, P., Bechtold, P., Beljaars, A. C. M., Berg L., Bidlot, J., Bormann, N., Delsol, C., Dragani, R., Fuentes, M., Geer, A. J., Haimberger, L., Healy, S. B., Hersbach, H., Holm, E. V., Isaksen, L., Kallberg, P., Kohler, M., Matricardi, M., NcNally, A.P., Monge-Sanz, B. M., Morcrette, J.-J., Park, B.-K., Peubey, C., Rosnay, P., Tavolato, C., Thepaut, J.-N., and Vitart F.: The ERA-Interim reanalysis: configuration and performance of the data assimilation system,Quart. J. R. Meteorol. Soc., 137, 553-597 (DOI: 10.1002/qj.828) , 2011。

Ding, Y. H., Liu, Y. M., Song, Y. J., Li, Q. Q.: Research and experiments of the dynamical model system for short-term climate prediction, Climatic Environ. Res., 7(2), 236–246, 2002 (in Chinese).

Eyring, V., Bony, S., Meehl, G. A., Senior, C. A., Stevens, B., Stouffer, R. J., Taylor, K. E.: Overview of the Coupled Model Intercomparison Project Phase 6 (CMIP6) experimental design and organization, Geosci. Model Dev., 9, 1937–1958, 2016, 2017.

Fetterer, F., Knowles, K., Meier, W., Savoie, M.: Sea Ice Index, digital media, National Snow and Ice Data Center. Boulder, CO., 2002.

Fyfe, J.C., Meehl, G.A., England, M.H., Mann, M. E. Santer, B. D., Flato, G. M., Hawkins, E., Gillett, N. P., Xie, S.–P., Kosaka, Y., Swart, N. C.: Making sense of the early-2000s warming slowdown, Nat. Clim. Change 6, 224–228, 2016.

Griffies, S. M., Gnanadesikan, A., Dixon, K. W., Dunn e, J. P., Gerdes, R., Harrison, M. J., Rosati, A., Lin, J., Bonita, R., Samuels, L., Spelman, M. J., Winton, M., Zhang, R.J.: Formulation of an ocean model for global climate simulations, Ocean Sci., 1, 45–79, 2005.

Gregory, J. M., Ingram, W. J., Palmer, M. A., Jones, G. S., Stott, P. A., Thorpe, R. B., Lowe, J. A., Johns, T. C., and Williams, K. D.: A new method for diagnosing radiative forcing and climate sensitivity, Geophys. Res. Lett., 31, L03205, doi:10.1029/2003GL018747, 2004.

Gregory, J.M., Webb, M. J., and Taylor, K. E.: Forcing, feedbacks and climate sensitivity in CMIP5 coupled atmosphere-ocean climate models, Geophys. Res. Lett., 39, L09712, doi:10.1029/2012GL051607, 2012.

Gent, P. R., Mcwilliams, J. C.: Isopycnal mixing in ocean circulation Models[J]. Journal of Physical Oceanography, 20(1), 150–155, 1990.

Guenther, A. B., Jiang, X., Heald, C. L., Sakulyanontvittaya, T., Duhl, T., Emmons, L. K., and Wang, X.: The Model of Emissions of Gases and Aerosols from Nature Version 2.1 (MEGAN2.1): An Extended and Updated Framework for Modeling Biogenic Emissions, Geoscientific Model Development 5(6): 1471–1492, 2012.

Hack, J. J., Parameterization of moist convection in the National Center for Atmospheric Research Community

Climate Model (CCM2), J. Geophys. Res., 99, 5551–5568, 1994.

Haarsma, R. J., Roberts, M. J., Vidale, P. L., Senior, C. A., Bellucci, A., Bao, Q., Chang, P., Corti, S., Fuckar, N. S., Guemas, V., Hardenberg, J. von, Hazeleger, W., Kodama, C., Koenigk, T., Leung, L. R., Lu, J., Luo, J. –J., Mao, J., Mizielinski, M. S., Mizuta, R. Nobre, P., Satoh, M., Scoccimarro, E., Semmler, T., Small, J., and Storch, J.–S. von : High Resolution Model Intercomparison Project (HighResMIP v1.0) for CMIP6, Geosci. Model Dev., 9, 4185–4208, doi:10.5194/gmd-9-4185-2016, 2016.

Holtslag, A. A. M., and Boville, B. A.: Local versus nonlocal boundary-layer diffusion in a global climate model, J. Climate, 6, 1825–1842, 1993.

Huffman, G., Bolvin, D., Braithwaite, D., Hsu, K., Joyce, R., Xie, P.: Integrated Multi-satellitE Retrievals for GPM (IMERG), version 4.4. NASA's Precipitation Processing Center, accessed 31 March, 2015, ftp://arthurhou.pps.eosdis.nasa.gov/gpmdata/, 2014.

IPCC Climate Change: The Physical Science Basis (eds Stocker, T. F., Qin, D., Plattner, G.-K., Tignor, M., Allen, S. K., Boschung, J., Nauels, A., Xia, Y., Bex V., and Midgley, P. M.) , Cambridge Univ. Press, Cambridge, United Kingdom and New York, NY, USA, 2013.

Ji, J.: A climate-vegetation interaction model: Simulating physical and biological processes at the surface, Journal of Biogeography, 22, 2063-2069, 1995.

Ji, J., Huang, M., and Li, K.: Prediction of carbon exchange between China terrestrial ecosystem and atmosphere in 21st century, Sci. China Ser. D: Earth Sci., 51(6), 885-898, 2008.

Li, J. D., Wang, W.-C., Liao, H., and Chang, W. Y.: Past and future direct radiative forcing of nitrate aerosol in East Asia, Theoretical and Applied Climatology, 121, 445-458, 2015.

Jiang X., Waliser, D. E.Xavier, P.K., Petch, J., Klingaman, N. P., Woolnough, S.J., Guan, B., Bellon, G., Crueger, T., DeMott, C., Hannay, C., Lin, H., Hu, W., Kim, D., Lappen, C., Lu, M.–M., Ma, H.-Y., Miyakawa, T., Ridout, J. A., Schubert, S.D., Scinocca, J., Seo, K.-H., Shindo, E., Song, X., Stan, C., Tseng, W.-L., Wang, W., Wu, T., Wyser, K., Wu, X., Zhang, G. J., Zhu, H.: Exploring Key Processes of the Madden-Julian Oscillation (MJO): A Joint WGNE MJO Task Force / GEWEX GASS Project on the Vertical Structure and Diabatic Processes of the MJO – Part I. Climate Simulations, J. Geophys. Res. Atmos., 120, 4718–4748. doi:10.1002/2014JD022375, 2015.

Jin, X., Wu, T., Li, L.: The quasi-stationary feature of nocturnal precipitation in the Sichuan Basin and the role of the Tibetan Plateau, Climate Dynamics, 41: 977-994. DOI: 10.1007/s00382-012-1521-y, 2013.

Jones, C.D., Arora, V., Friedlingstein, P., Bopp, L., Brovkin, V., Dunne, J., Graven, H., Hoffman, F., Ilyina, T., John, J. G., Jung, M., Kawamiya, M., Koven, C., Pongratz, J., Raddatz, T., Randerson, J. T., and Zaehle, S.: C4MIP – The Coupled Climate–Carbon Cycle Model Intercomparison Project: experimental protocol for CMIP6, Geosci. Model Dev., 9, 2853–2880, doi:10.5194/gmd-9-2853-2016, 2016.

Klein, S. A., and Hartmann, D. L.: The seasonal cycle of low stratiform clouds, J. Climate, 6, 1587–1606, 1993.

Kristj´ansson, J. E., and Kristiansen, J.: Impact of a new scheme for optical properties of ice crystals on climates of two gcms, J. Geophys. Res., 105, 10063–10079, 2000.

Lamarque, J.-F., Emmons, L. K., Hess, P. G., Kinnison, D. E., Tilmes, S., Vitt, F., Heald, C. L., Holland, E. A., Lauritzen, P. H., Neu, J., Orlando, J. J., Rasch, P. J., and Tyndall, G. K.: CAM-chem: description and evaluation of interactive atmospheric chemistry in the Community Earth System Model, Geosci Model Dev, 5, 369-411, 2012.

Large, W. G., McWilliams, J. C., and Doney, S. C.: Oceanic vertical mixing: A review and a model with a nonlocal boundary layer parameterization, Rev. Geophys., 32, 363-403, 1994.

Liu, Y., and Daum, P. H.: Indirect warming effect from dispersion forcing, Nature, 419, 580-581, 2002.

Liou, K. N.: An Introduction to Atmospheric Radiation, China Meteorological Press, 313-327 (in Chinese), 2004.

Loeb, N.G., Lyman, J.M., Johnson, G.C,, Allan, R.P., Doelling, D.R., Wong, T., Soden, B.J., and Stephens, G.L.: Observed changes in top-of-the-atmosphere radiation and upper-ocean heating consistent within uncertainty, Nature Geosciences, DOI 10.1038/NGE, 2012.

Lu, Y., Zhou, M., and Wu, T.: Validation of parameterizations for the surface turbulent fluxes over sea ice with CHINARE 2010 and SHEBA data, Polar Research, 32, 20818, http://dx.doi.org/10.3402/polar.v32i0.20818, 2013.

Medhaug, I., Martin, B. S., Erich, M. F., and Knutti, R.: Reconciling controversies about the 'global warming hiatus', Nature, 545, 41–47, 2017.

Morice, C, P., Kennedy, J. J., Rayner, N.A., and Jones, P.D.: Quantifying uncertainties in global and regional temperature change using an ensemble of observational estimates: The HadCRUT4 data set, J. Geophys. Res. 117, D08101, 2012.

Martin, G.M., Johnson, D.W., and Spice, A.: The measurement and parameterisation of effective radius of droplets in warm stratocumulus clouds, J. Atmos. Sci., 51, 1823–1842, 1994.

McFarlane, N. A.: The effect of orographically excited gravity wave drag on the general circulation of the lower stratosphere and troposphere, J. Atmos. Sci., 44, 1775-1800, 1987.

Oleson, K. W., Lawrence, D. M. and Dai, Y. J.: Technical description of the Community Land Model (CLM), NCAR Technical Note NCAR/TN-461+STR, 2004.

Pontikis, C.A., and Hicks, E.; Contribution to the cloud droplet effective radius parameterization, Geophys. Res. Lett. 19, 2227–2230, 1992.

Peng, Y., and Lohmann, U.: Sensitivity study of the spectral dispersion of the cloud droplet size distribution on the indirect aerosol effect, Geophys. Res. Lett., 30(10), 1507, doi:10.1029/2003GL017192, 2003.

Quaas J, Boucher O, and Lohmann U: Constraining the total aerosol indirect effect in the LMDZ and ECHAM4 GCMs using MODIS satellite data. Atmos Chem Phys 6,947-955, 2006

Rasch, P. J., and Kristj´ansson, J. E.: A comparison of the CCM3 model climate using diagnosed and predicted condensate parameterizations, J. Climate, 11, 1587-1614, 1998.

Rahmstorf, S.: A fast and complete convection scheme for ocean models, Ocean Modelling, 101, 9–11, 1993.

Rayner, N. A., Parker, D. E., Horton, E. B., Folland, C., Alexander, L., Rowell, D., Kent, E., and Kaplan, A.: Global analyses of sea surface temperature, sea ice, and night marine air temperature since the late nineteenth century, Journal of Geophysical Research, 108(D14), 4407, doi:10.1029/2002JD002670, 2003.

Richter, J. H., Sassi, F., and Garcia, R. R.: Toward a physically based gravity wave source parameterization in a general circulation model, J. Atmos. Sci., 67, 136--156, 2010.

Sweeney, C., Gnanadesikan, A., Griffies, S. M., Harrison, M., Rosati, A., Samuels, B.: Impacts of shortwave penetration depth on large-scale ocean circulation and heat transport, Journal of Physical Oceanography 35, 1103–1119, 2005.

Stevens, B., Fiedler, S., Kinne, S., Peters, K., Rast, S., Musse, J., Smith, S.J., and Mauritsen, T.: MACv2-SP: a parameterization of anthropogenic aerosol optical properties and an associated Twomey effect for use in CMIP6, Geos.Mod.Dev.,10, 433-452, 2017.

Tan, H.H., Zhang, L.J., Chu, M., Wu, T.W., Qiu, B., and Li, J.L.: An analysis of simulated global sea ice extent, thickness, and causes of error with the BCC_CSM model. Chinese Journal of Atmospheric Sciences (in Chinese), 39 (1): 197−209, 2015.

Taylor, K. E., Stouffer, R. J., and Meehl, G. A.: An Overview of Cmip5 and the Experiment Design, B. Am. Meteorol. Soc., 93, 485–498, 2012.

Tietsche, S., Balmaseda, M., Zuo, H., Mogensen, K.: Arctic sea ice in the ECMWF MyOcean2 ocean reanalysis ORAP5. Tech Rep 737, European Center for Medium-Range Weather Forecasts, Reading, UK, 2014.

Wielicki, B.A., Barkstrom, B. R., Harrison, E. F., Lee, R. B., Smith, G. L., and Cooper, J. E.: Clouds and the earth's radiant energy system (CERES): an earth observing system experiment, Bull. Am. Meteorol. Soc., 77,

Geosci. Model Dev. Discuss., https://doi.org/10.5194/gmd-2018-254
Manuscript under review for journal Geosci. Model Dev.
Discussion started: 13 November 2018

Geoscientific Model Development
Open Access
Discussions

853–868, 1996.

Winton, M.: A reformulated three-layer sea ice model, J. Atmo.Oceanic Technol., 17, 525–531, 2000.

Wu, T., Song, L., Li, W., Wang, Z., Zhang, H., Xin, X., Zhang, Y., Zhang, L., Li, J., Wu, F., Liu, Y., Zhang, F., Shi, X., Chu, M., Zhang, J., Fang, Y., Wang, F., Lu,Y., Liu, X., Wei, M., Liu, Q., Zhou, W., Dong, M., Zhao, Q., Ji, J., Li, L., and Zhou, M.: An overview of BCC climate system model development and application for climate change studies, J. Meteor. Res., 28(1), 34-56, 2014.

Wu, T., Li, W., Ji, J., Xin, X., Li, L., Wang, Z., Zhang, Y., Li, J., Zhang, F., Wei, M., Shi, X., Wu, F., Zhang, L., Chu, M., Jie, W., Liu, Y.,Wang, F., Liu, X., Li, Q., Dong, M., Liang, X., Gao, Y., and Zhang, J.: Global carbon budgets simulated by the Beijing climate center climate system model for the last century, J Geophys Res Atmos, 118, 4326-4347. doi: 10.1002/jgrd.50320, 2013.

Wu, T.: A Mass-Flux Cumulus Parameterization Scheme for Large-scale Models: Description and Test with Observations, Clim. Dyn., 38:725–744, DOI: 10.1007/ s00382-011-0995-3, 2012.

Wu, T., Yu, R., Zhang, F., Wang, Z., Dong, M., Wang, L., Jin, X., Chen, D.L., and Li, L.： The Beijing Climate Center atmospheric general circulation model: description and its performance for the present-day climate, Climate Dynamics, 34, 123-147, DOI 10.1007/s00382-008-0487-2, 2010.

Wu, T., Yu, R., and Zhang, F.: A modified dynamic framework for atmospheric spectral model and its application, J. Atmos.Sci., 65, 2235-2253, 2008

Wu, T., and Wu, G.: An empirical formula to compute snow cover fraction in GCMs, Adv.Atmos.Sci., 21, 529-535, 2004.

Xia, K., Luo, Y., and Li, W. P.: Simulation of freezing and melting of soil on the northeast Tibetan Plateau. Chinese Sci. Bull., 56, 1-4, doi: 10.1007/s11434-011-4542-8, 2011.

Xin, X., Wu, T., and Zhang, J.: Introduction of CMIP5 experiments carried out with the climate system models of Beijing Climate Center, Adv. Clim. Change Res., 4(1), 41-49， doi: 10.3724/SP.J.1248.2013.041, 2013.

Xu, K. M., and Krueger, S. K.: Evaluation of cloudiness parameterizations using a cumulus ensemble model, Mon. Wea. Rev., 119, 342–367, 1991.

Xu, L., and Penner, J.E.: Global simulations of nitrate and ammonium aerosols and their radiative effects, Atmos. Chem. Phys., 12, 9479-9504, 2012.

Zeng, X., Zhao, M., and Dickinson, R. E.: Intercomparison of bulk aerodynamic algorithms for the computation of sea surface fluxes using TOGA COARE and TAO data, J. Climate, 11, 2628-2644, 1998.

Zeng, X., Zhang, Q., Johnson, D., and Tao, W.-K.: Parameterization of wind gustiness for the computation of

Geosci. Model Dev. Discuss., https://doi.org/10.5194/gmd-2018-254
Manuscript under review for journal Geosci. Model Dev.
Discussion started: 13 November 2018

Geoscientific Model Development Discussions
Open Access

ocean surface fluxes at different spatial scales, Monthly Weather Review, 130, 2125-2133, 2002.

Zhang, G.J.: Convective quasi-equilibrium in midlatitude continental environment and its effect on convective parameterization. J Geophys Res 107(D14), doi:10.1029/2001JD001005, 2002.

Zhang, M., Lin, W., Bretherton, C. S., Hack, J. J., and Rasch, P. J.: A modified formulation of fractional stratiform condensation rate in the NCAR community atmospheric model CAM2, J. Geophys. Res., 108 (D1), 2003.

Zhang, Y., Gao, Z., Li, D., Li, Y., Zhang, N., Zhao, X., and Chen, J.: On the computation of planetary boundary-layer height using the bulk Richardson number method, Geosci. Model Dev., 7, 2599–2611, 2014.

Zhou, W.Y., Luo, Y., Li, W.P., Shi, X.L., and Zhang, Y: Comparative studies of different radiation schemes within vegetation in land model, Chinese Science Bulletin, 63, 10.1360/N972018-00398, 2018.

Geosci. Model Dev. Discuss., https://doi.org/10.5194/gmd-2018-254
Manuscript under review for journal Geosci. Model Dev.
Discussion started: 13 November 2018

Geoscientific Model Development
Discussions
Open Access
EGU

Table 1. BCC models for CMIP5 and CMIP6

Model versions	Atmosphere	Atmos Chemistry and Aerosol	Land Surface	Ocean	Sea Ice
BCC-CSM1.1 in CMIP5 (Wu et al., 2013)	BCC-AGCM2.1 (1) T42，26 layers (2) Top at 2.917 hPa	(1) Prescribed aerosols (2) No atmospheric chemistry (3) Global carbon budget without spatial distribution	BCC-AVIM1.0	MOM4-L40v1 (1) Tri-polar: 0.3 to 1 deg latitude x 1 deg longitude, and 40 layers (2) Oceanic carbon cycle based on OCMIP2	SISv1
BCC-CSM1.1m in CMIP5 (Wu et al., 2013)	BCC-AGCM2.2 (1) T106，26 layers (2) Top at 2.917 hPa	Same as BCC-CSM1.1	BCC-AVIM1.0	MOM4-L40v2	SISv2
BCC-CSM2-MR In CMIP6	BCC-AGCM3-MR (1) T106，46 layers (2) Top at 1.459 hPa	(1) Prescribed aerosols (2) No atmospheric chemistry (3) Prognostic spatial CO_2 in the atmosphere	BCC-AVIM2.0	MOM4-L40v2	SISv2
BCC-CSM2-HR In CMIP6	BCC-AGCM3-HR (1) T266，56 layers (2) Top at 0.092 hPa	(1) Prescribed aerosols (2) No atmospheric chemistry	BCC-AVIM2.0	MOM4-L40v2	SISv2
BCC-ESM1 In CMIP6	BCC-AGCM3-Chem (1) T42，26 layers (2) Top at 2.917 hPa	(1) Prognostic aerosols (2) MOZART2 atmospheric chemistry	BCC-AVIM2.0	MOM4-L40v2	SISv2

Geosci. Model Dev. Discuss., https://doi.org/10.5194/gmd-2018-254
Manuscript under review for journal Geosci. Model Dev.
Discussion started: 13 November 2018

Geoscientific Model Development Discussions
Open Access

Table 2. Main physics schemes in atmospheric components (BCC-AGCM) of BCC-CSM versions for CMIP5 and CMIP6

	BCC-AGCM2 for CMIP5	**BCC-AGCM3 for CMIP6**
Deep convection	The cumulus convection parameterization scheme (Wu, 2012)	A modified Wu'2012 scheme described in this work
Shallow/Middle Tropospheric Moist Convection	Hack (1994)	Hack (1994)
Cloud macrophysics	Cloud fraction diagnosed from updraft mass flux and relative humidity (Collins et al., 2004)	A new scheme to diagnose cloud fraction described in this work
Cloud microphysics	Modified scheme of Rasch and Kristj´ansson (1998) by Zhang et al. (2003). No aerosol indirect effects	Modified scheme of Rasch and Kristj´ansson (1998) by Zhang et al. (2003), but included the aerosol indirect effects in which liquid cloud droplet number concentration is diagnosed using the aerosols masses.
gravity wave drag	Gravity wave drag only generated by orography (Mcfarlane 1987)	Gravity wave drag generated by both orography (Mcfarlane 1987) and convection (Beres et al., 2004) using tuned parameters related to model resolutions.
Radiative transfer	Radiative transfer scheme used in CAM3 (Collins et al., 2004) with no aerosol indirect effects, and cloud drop effective radius for clouds is only function of temperature and has a distinct difference between maritime, polar, and continental for warm clouds.	Radiative transfer scheme used in CAM3 (Collins et al., 2004), but including the aerosol indirect effects, and the effective radius of the cloud drop for liquid clouds is diagnosed using liquid cloud droplet number concentration.
Boundary Layer	ABL parameterization [Holtslag and Boville, 1993]	ABL parameterization [Holtslag and Boville, 1993], but modified PBL height computation referred to Zhang et al. (2014)

Geosci. Model Dev. Discuss., https://doi.org/10.5194/gmd-2018-254
Manuscript under review for journal Geosci. Model Dev.
Discussion started: 13 November 2018

Table 3. Main physics schemes in BCC-AVIM versions

BCC-AVIM1.0 in CMIP5	BCC-AVIM2.0 in CMIP6
◆ Soil-Vegetation-Atmosphere Transfer module	◆ Modified freeze-thaw scheme for soil water (below 0 degree and dependent on soil & water) (Xia et al., 2011)
◆ Multi-layer snow-soil scheme (same as NCAR CLM3)	◆ Improved parameterization of snow surface albedo (Chen et al., 2014) and snow cover fraction (Wu and Wu, 2004)
◆ Snow Cover Fraction scheme (sub-grid topography)	◆ Four-stream radiation transfer through vegetation canopy (Zhou et al., 2018)
◆ Vegetation growth module	◆ A vegetation phenology similar to Canadian Terrestrial Ecosystem Model (Arora and Boer, 2005)
◆ Soil carbon decomposition module	◆ Parameterized rice paddy scheme
◆ Land use change module (variable crop planting area)	◆ land VOC module (Guenther et al., 2012)

Geosci. Model Dev. Discuss., https://doi.org/10.5194/gmd-2018-254
Manuscript under review for journal Geosci. Model Dev.
Discussion started: 13 November 2018

Geoscientific Model Development Discussions
Open Access

Table 4. Energy balance and cloud radiative forcing at the top-of-atmosphere (TOA) in the model with contrast to CERES/EBAF and CERES observations. Units: W m^{-2}.

	BCC-CSM2-MR (CMIP6)	BCC-CSM1.1m (CMIP5)	CERES/EBAF (OBS)	CERES (OBS)
Net energy at TOA	0.85	0.98		
TOA outgoing longwave radiative flux	239.15	236.10	239.72	238.95
TOA incoming shortwave Radiation	340.46	341.70	340.18	341.47
TOA net shortwave radiative flux	239.09	235.96	240.53	244.68
TOA outgoing longwave radiative flux in clear sky	265.02	265.58	265.80	266.87
TOA net shortwave radiative flux in clear sky	288.67	288.71	287.68	294.69
Shortwave cloud radiative forcing	-49.55	-52.71	-47.16	-48.58
Longwave cloud radiative forcing	25.87	29.48	26.07	27.19

Notes: The model data are the mean of 1981 to 2014, while the available observation data are for 2003–2014.

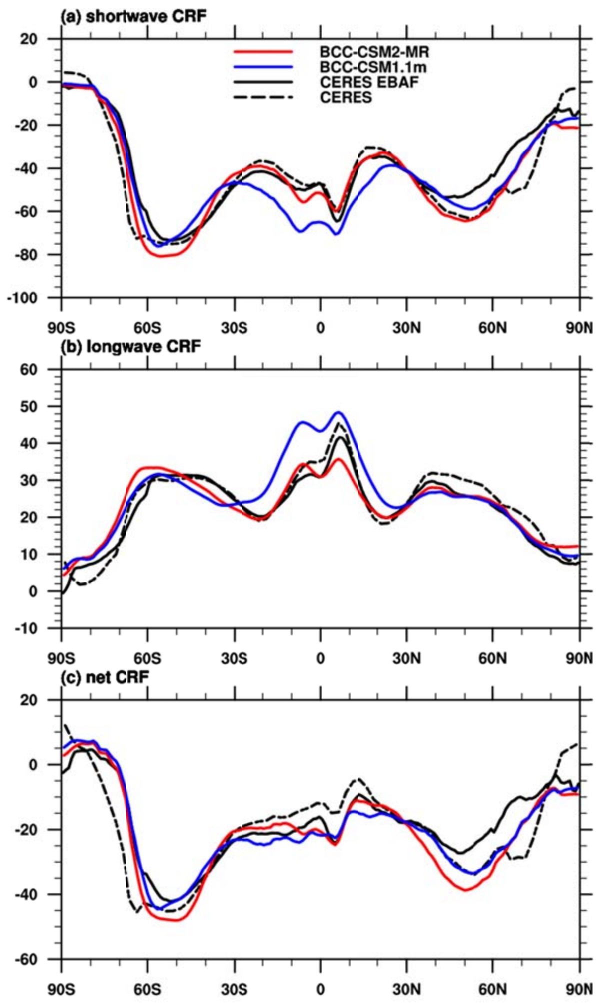

Figure 1. Zonal averages of the cloud radiative forcing from the BCC CMIP5 and CMIP6 models and observations (in W m^{-2}; top row: shortwave effect; middle row: longwave effect; bottom row: net effect). Model results are for the period 1985–2005, while the available CERES ES-4 and CERES EBAF 2.6 data set are for 2003–2014.

Geosci. Model Dev. Discuss., https://doi.org/10.5194/gmd-2018-254
Manuscript under review for journal Geosci. Model Dev.
Discussion started: 13 November 2018

Geoscientific Model Development Discussions
Open Access
EGU

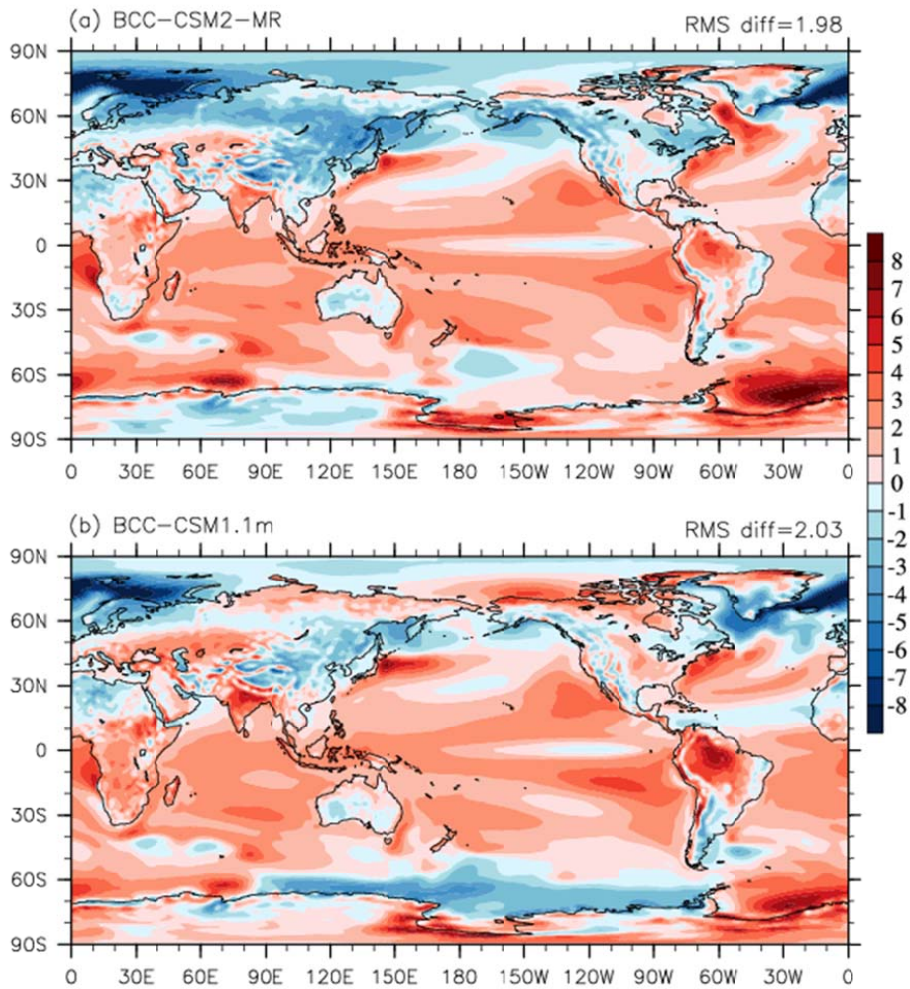

Figure 2. Annual-mean surface (2 meter) air temperature biases (°C) of (a) BCC-CSM2-MR and (b) BCC-CSM1.1m simulations with contrast to the reanalysis ERA-Interim for the period of 1986 to 2005.

Geosci. Model Dev. Discuss., https://doi.org/10.5194/gmd-2018-254
Manuscript under review for journal Geosci. Model Dev.
Discussion started: 13 November 2018

Geoscientific Model Development Discussions
Open Access

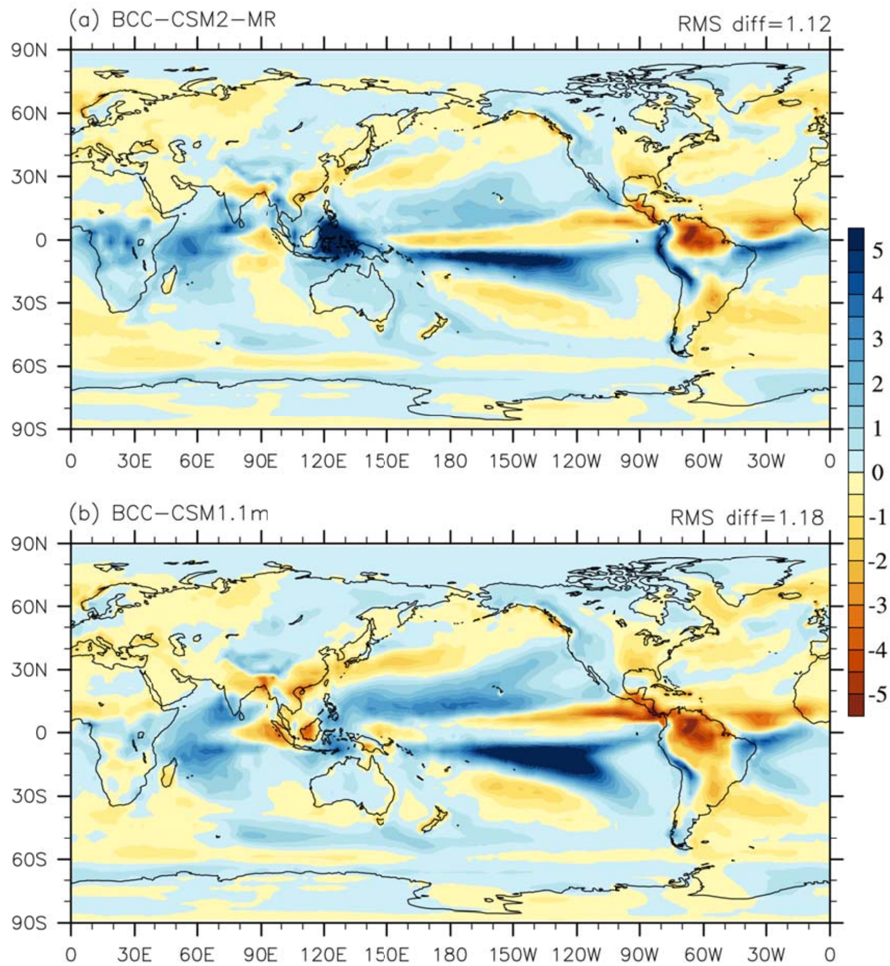

Figure 3. Annual-mean precipitation rate biases (mm day^{-1}) of (a) BCC-CSM2-MR and (b) BCC-CSM1.1m simulations with contrast to 1986-2005 precipitation analyses from the Global Precipitation Climatology Project (Adler et al., 2003)

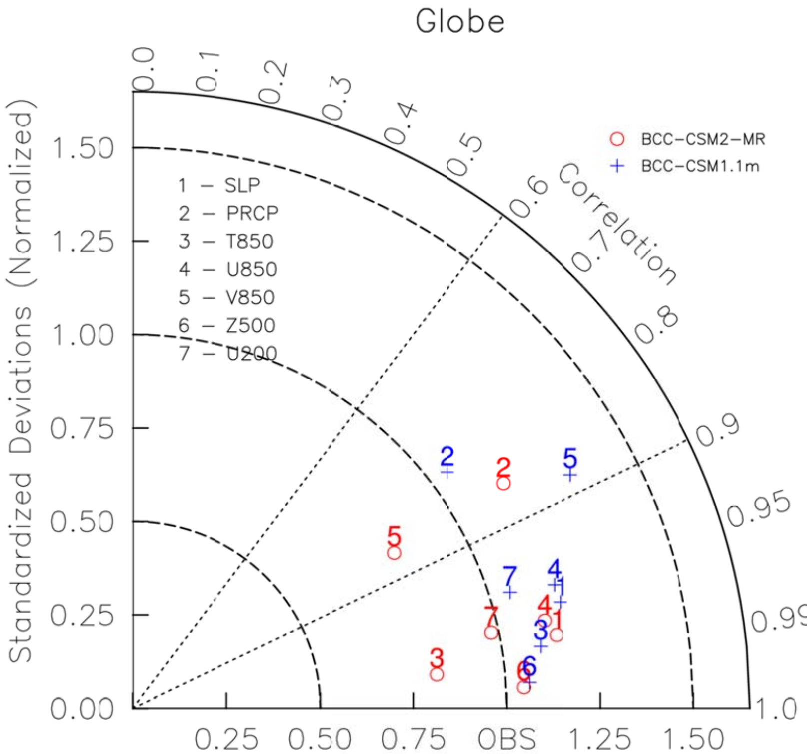

Figure 4. Taylor diagram for the global climatology (1980–2005) of sea level pressure (SLP), precipitation (PRCP), temperature at 850 hPa (T850), zonal wind at 850 hPa (U850), longitudinal wind at 850 hPa (V850), geopotential height at 500 hPa (Z500), and zonal wind at 200 hPa (U200). The radial coordinate shows the standard deviation of the spatial pattern, normalized by the observed standard deviation. The azimuthal variable shows the correlation of the modelled spatial pattern with the observed spatial pattern. Analysis is for the whole globe. The reference dataset is NCEP. The model results of BCC-CSM2-MR and BCC-CSM1.1m are the mean for 1980 to 2000. Blue crosses are for BCC-CSM1.1m and circles for BCC-CSM2-MR.

Geosci. Model Dev. Discuss., https://doi.org/10.5194/gmd-2018-254
Manuscript under review for journal Geosci. Model Dev.
Discussion started: 13 November 2018

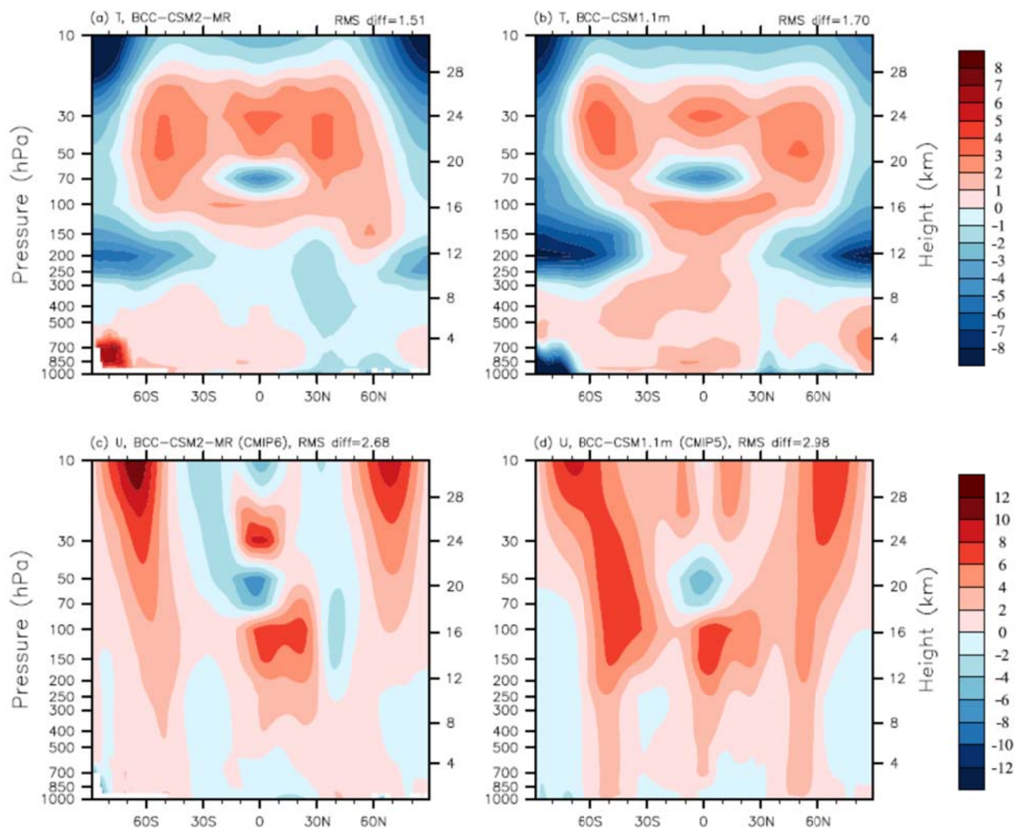

Figure 5. Pressure-latitude sections of annual mean temperature (top panels, K) and zonal wind (bottom, m s^{-1}) biases for BCC-CSM2-MR (left) and BCC-CSM1.1m (right), with respectto the reanalysis ERA-Interim for the period of 1986 to 2005.

Geosci. Model Dev. Discuss., https://doi.org/10.5194/gmd-2018-254
Manuscript under review for journal Geosci. Model Dev.
Discussion started: 13 November 2018

Geoscientific Model Development Discussions
Open Access

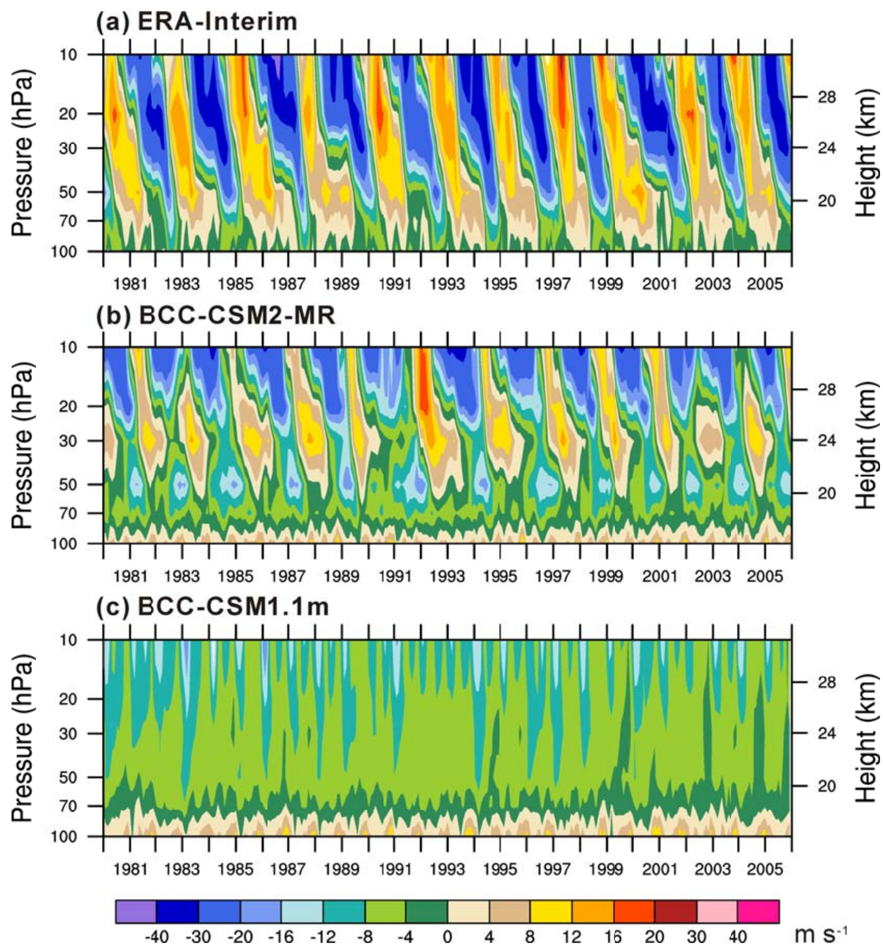

Figure 6. Tropical zonal winds (m s-1) between 5°S and 5°N in the lower stratosphere from 1980 to 2005 for (a) ERA-Interim reanalysis, (b) BCC-CSM2-MR, and (c) BCC-CSM1.1m.

Geosci. Model Dev. Discuss., https://doi.org/10.5194/gmd-2018-254
Manuscript under review for journal Geosci. Model Dev.
Discussion started: 13 November 2018

Geoscientific Model Development Discussions
Open Access

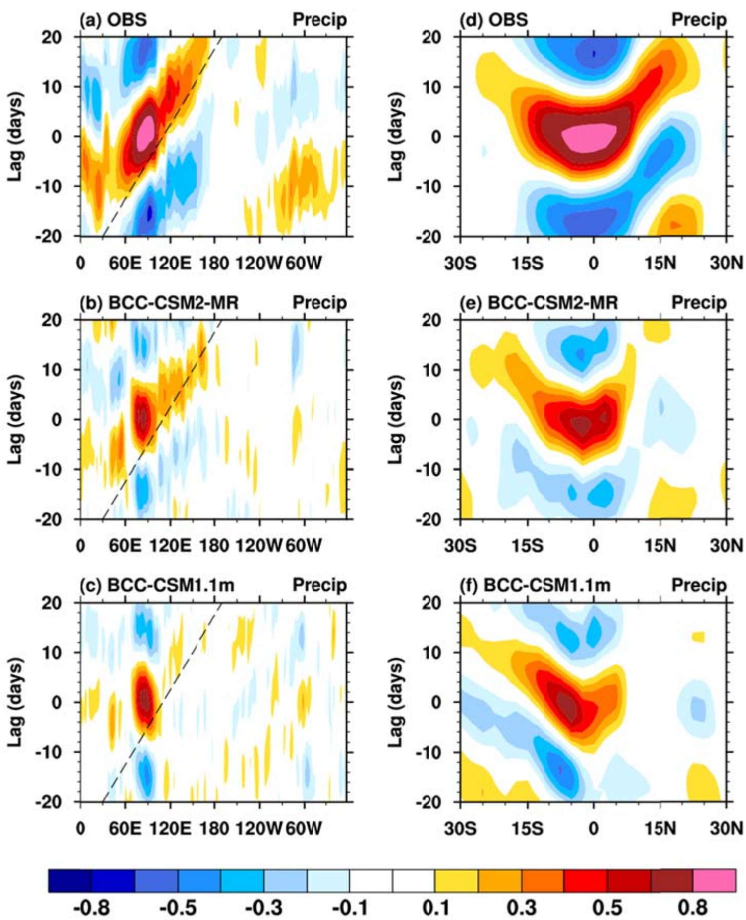

Figure 7. Left panels: longitude-time evolution of lagged correlation coefficient for the 20–100 day band-pass-filtered anomalous rainfall (averaged over 10°S–10°N) against itself averaged over the equatorial eastern Indian Ocean (75°–85°E; 5°S–5°N). Dashed lines in each panel denote the 5 m s^{-1} eastward propagation speed. The reference GPCP is from 1997-2005. Models are from their historical simulations. Right panels: same as in the left panels, but for latitude-time sections showing meridional propagation of the filtered rainfalls.

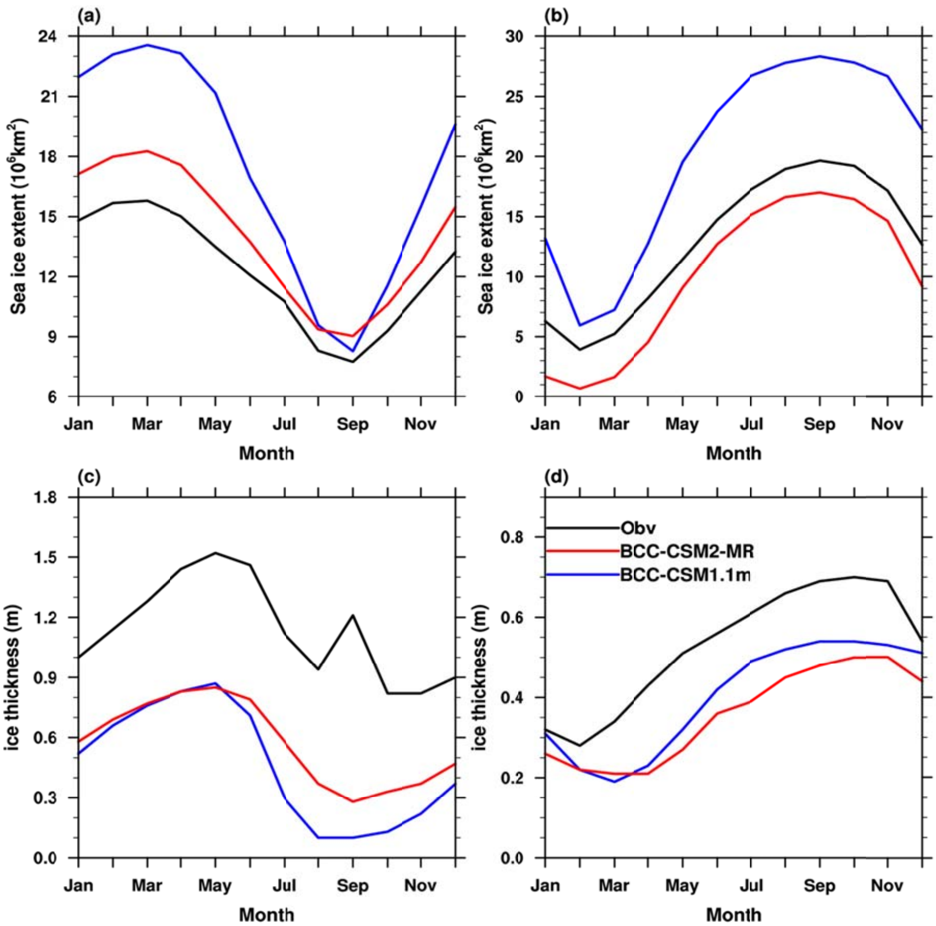

Figure 8. Mean (1980–2005) seasonal cycle of sea-ice extent (upper panel, the ocean area with a sea-ice concentration of at least 15%) and mean thickness (lower panel) in the Northern Hemisphere (left) and the Southern Hemisphere (right). The observed seasonal cycles (1980–2005) of sea-ice extent are based on the National Snow and Ice Data Center (NSIDC; Fetterer et al., 2002) data sets and ice thickness based on European Center for Medium-Range Weather Forecast (Tietsche, et al., 2014).

Geosci. Model Dev. Discuss., https://doi.org/10.5194/gmd-2018-254
Manuscript under review for journal Geosci. Model Dev.
Discussion started: 13 November 2018

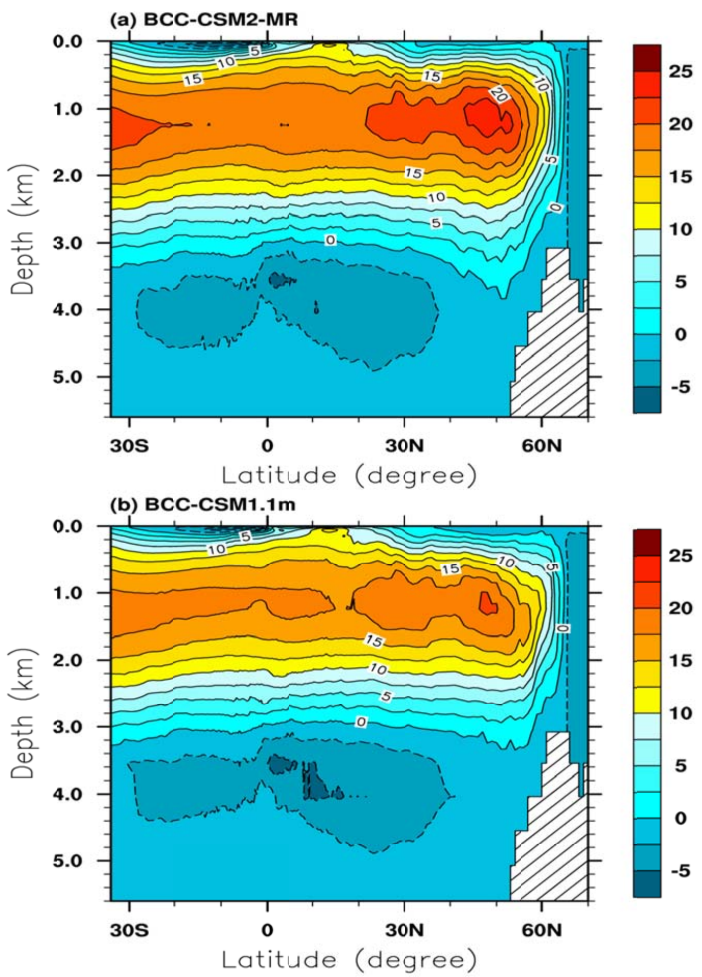

Figure 9. Zonally-averaged streamfunction of the Atlantic Meridional Overturning Circulation (AMOC) for the period of 1980 to 2005 in BCC-CSM2-MR (top) and BCC-CSM1.1m (bottom). Units: Sv

Geosci. Model Dev. Discuss., https://doi.org/10.5194/gmd-2018-254
Manuscript under review for journal Geosci. Model Dev.
Discussion started: 13 November 2018

Geoscientific Model Development
Discussions
Open Access

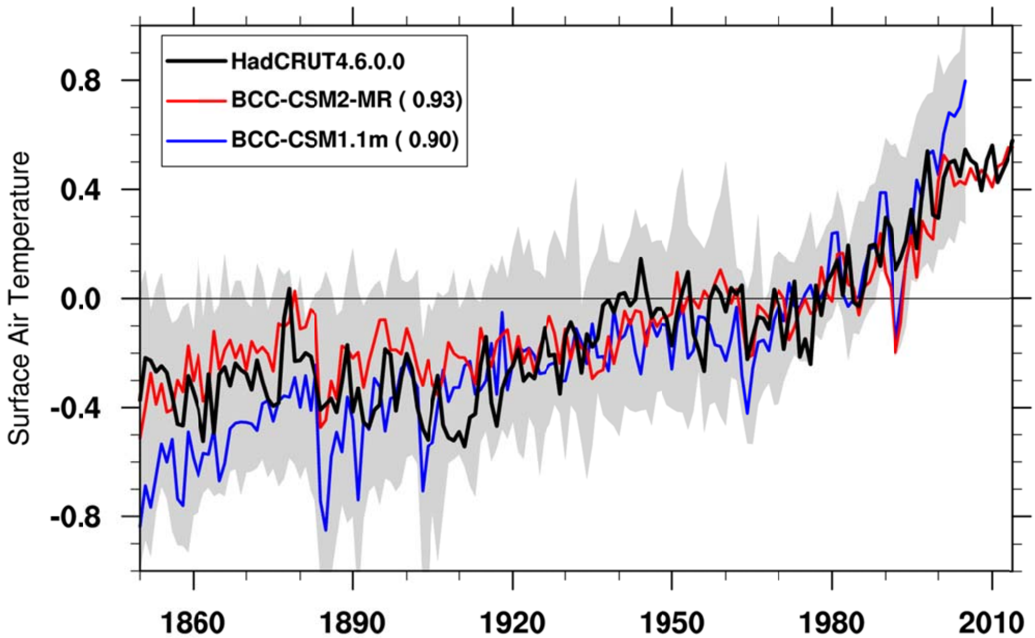

Figure 10. Time series of anomalies in the global (60°S to 60°N) mean surface air temperature from 1850 to 2014. The reference climate to deduce anomalies is for each individual curve from 1961 to 1990. The numbers in the bracket denote the correlation coefficient of 11-year smoothed BCC model data with the HadCRUT4.6.0.0 (Morice et al., 2012) observation. Dashed area shows the spread of CMIP5 model data.

Geosci. Model Dev. Discuss., https://doi.org/10.5194/gmd-2018-254
Manuscript under review for journal Geosci. Model Dev.
Discussion started: 13 November 2018

Geoscientific Model Development
Discussions

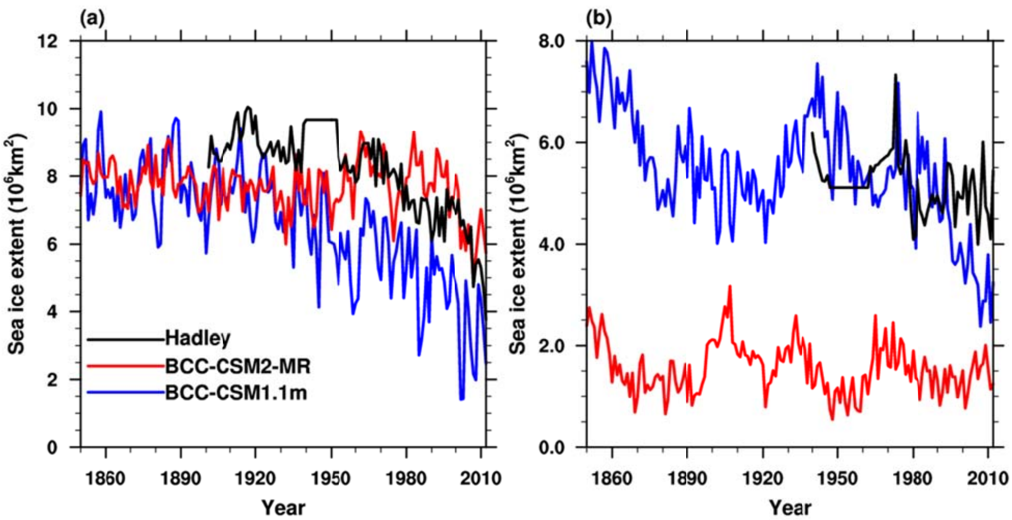

Figure 11. Time-series of sea-ice extent from 1851 to 2012 for (a) the Arctic in September and (b) the Antarctic in March as modelled in BCC-CSM2-MR and BCC-CSM1.1m and observations-based Hadley Centre Sea Ice and Sea Surface Temperature data set (Rayner et al., 2003).

Geosci. Model Dev. Discuss., https://doi.org/10.5194/gmd-2018-254
Manuscript under review for journal Geosci. Model Dev.
Discussion started: 13 November 2018

Geoscientific Model Development Discussions
Open Access

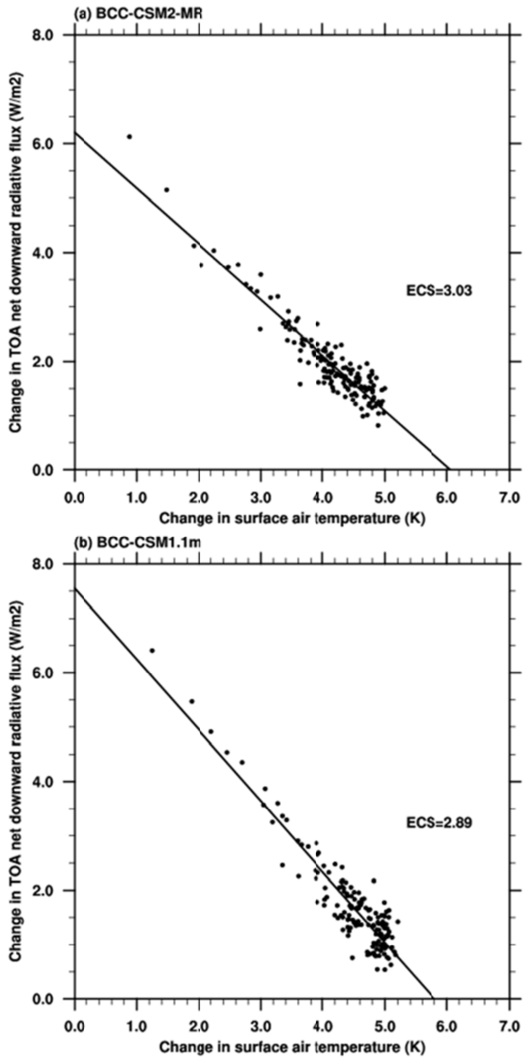

Figure 12. Relationships between the change in net top-of-atmosphere radiative flux and global-mean surface air temperature change simulated by abruptCO_2 relative to the pre-industrial control run.

Geosci. Model Dev. Discuss., https://doi.org/10.5194/gmd-2018-254
Manuscript under review for journal Geosci. Model Dev.
Discussion started: 13 November 2018

Geoscientific Model Development Discussions

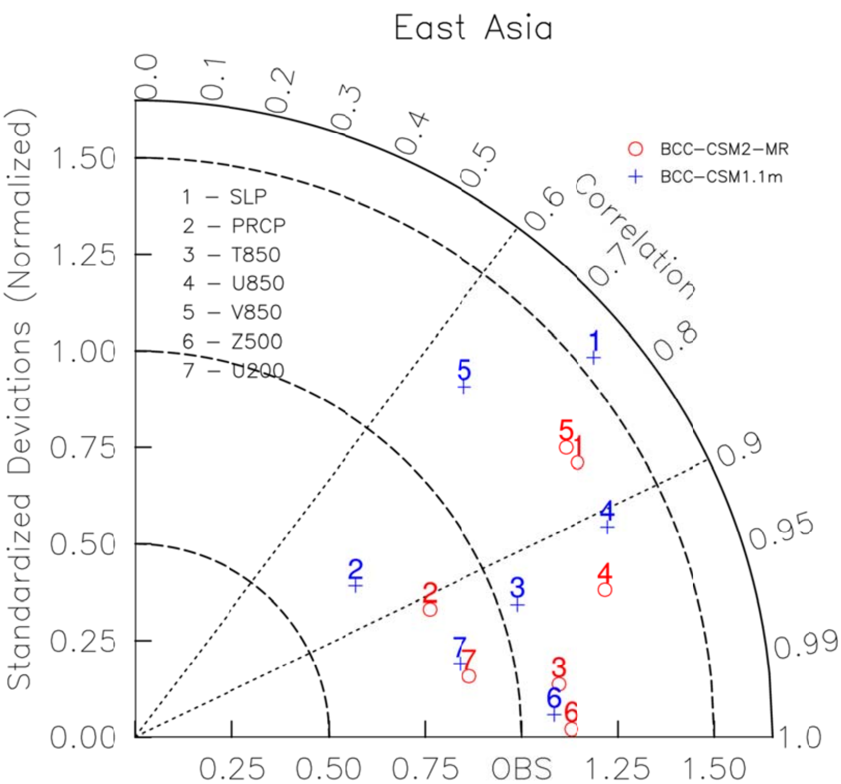

Figure 13. Same as in Figure 4, but for the domain covering East Asia (20°-50°N, 100°-140°E).

Geosci. Model Dev. Discuss., https://doi.org/10.5194/gmd-2018-254
Manuscript under review for journal Geosci. Model Dev.
Discussion started: 13 November 2018

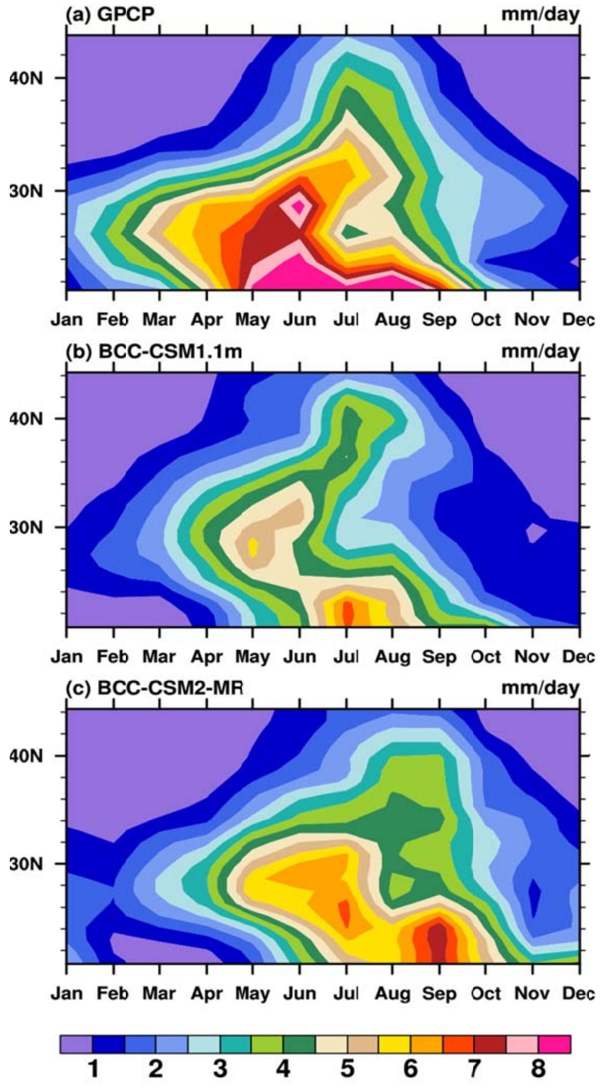

Figure 14. The variations of 100°-120°E averaged 1980-2005 monthly precipitation along each latitude from 20°N to 25°N with time. (a) GPCP, (b) BCC-CSM1.1m, (c) BCC-CSM2-MR.

Geosci. Model Dev. Discuss., https://doi.org/10.5194/gmd-2018-254
Manuscript under review for journal Geosci. Model Dev.
Discussion started: 13 November 2018

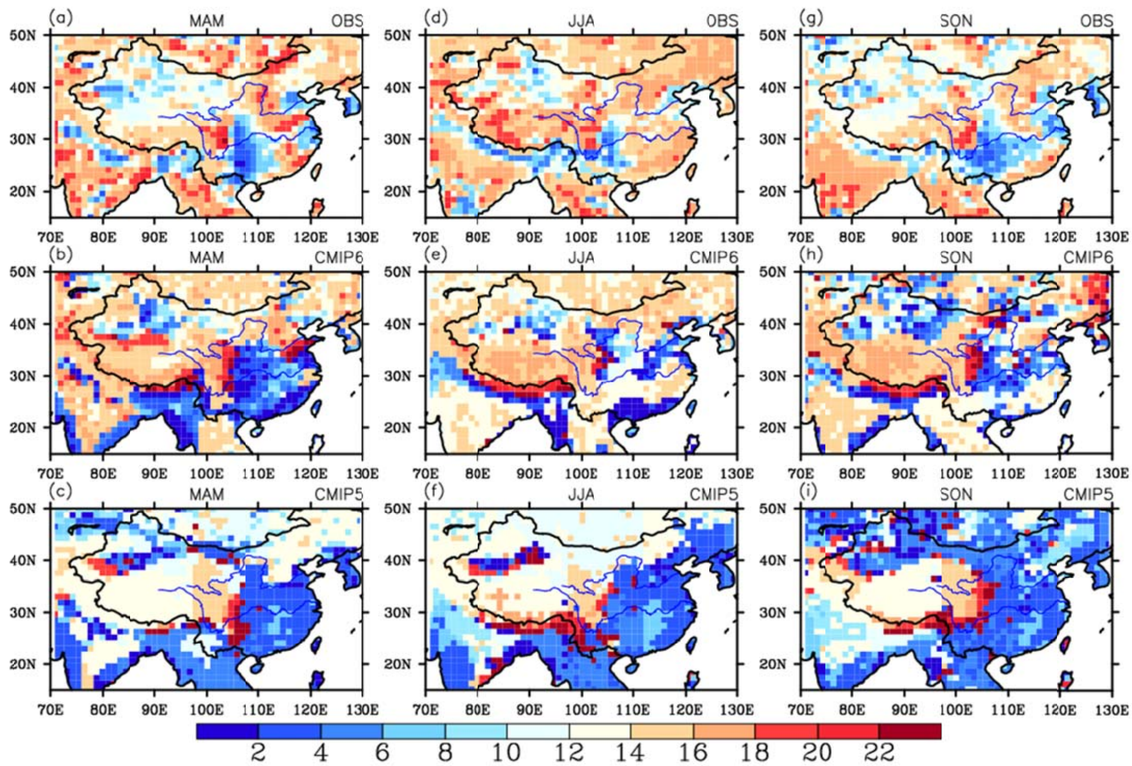

Figure 15. Local times of maximum frequency of rainfall occurrence over China and its surrounding areas. The rainfall occurrence is defined as the hourly precipitation larger than 1 mm for BCC-CSM2-MR (middle panel), BCC-CSM1.1m (bottom panel), and TRMM data (top panel, Huffman et al., 2014).